Modeling and Performance Analysis of GaSb-Based Mid-infrared Vertical Cavity Surface Emitting Laser

by

Md. Mahbub Hasan

A thesis submitted to the Department of Electrical and Electronic Engineering, Khulna University of Engineering & Technology (KUET) in partial fulfillment of the requirements for the degree
of
Master of Science in Electrical and Electronic Engineering

Department of Electrical and Electronic Engineering
Khulna University of Engineering & Technology
Khulna-9203, Bangladesh
May 2010

Declaration

This is to certify that the thesis work entitled "*Modeling and Performance Analysis of GaSb-Based Mid-infrared Vertical Cavity Surface Emitting Laser*" has been carried out by *Md.Mahbub Hasan* in the Department of *Electrical and Electronic Engineering*, Khulna University of Engineering & Technology, Khulna, Bangladesh. According to my knowledge the above thesis work or any part of this work has not been submitted anywhere for the award of any degree or diploma.

Khulna University of Engineering & Technology
KUET
Bangladesh
Central Library

Signature of Supervisor

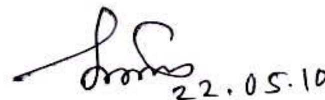

Signature of Candidate

Approval

This is to certify that the thesis work submitted by *Md. Mahbub Hasan* entitled "*Modeling and Performance Analysis of GaSb-Based Mid-infrared Vertical Cavity Surface Emitting Laser*" has been approved by the board of examiners for the partial fulfillment of the requirements for the degree of *Master of Science in Electrical and Electronic Engineering* in the Department of *Electrical and Electronic Engineering*, Khulna University of Engineering & Technology, Khulna, Bangladesh in May 2010.

BOARD OF EXAMINERS

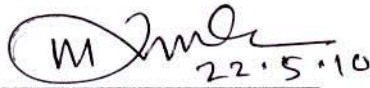

Dr. Md. Rafiqul Islam
Professor,
Department of Electrical and Electronic Engineering,
Khulna University of Engineering & Technology,
Khulna-9203, Bangladesh.

Chairman
(Supervisor)

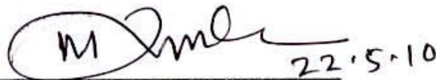

Head of the Department
Electrical and Electronic Engineering,
Khulna University of Engineering & Technology,
Khulna-9203, Bangladesh.

Member

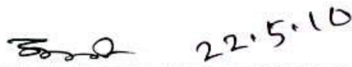

Prof. Dr. Md. Nurunnabi Mollah
Dean, Faculty of Engineering & Technology,
Eastern University,
Dhaka, Bangladesh.

Member

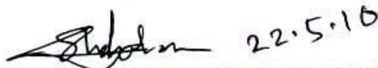

Dr. Md. Shahjahan
Associate Professor
Department of Electrical and Electronic Engineering,
Khulna University of Engineering & Technology,
Khulna-9203, Bangladesh.

Member

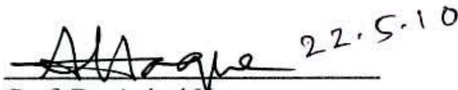

Prof. Dr. Anisul Haque
Chairperson,
Department of Electrical and Electronic Engineering,
East West University,
Dhaka, Bangladesh.

Member (External)

Acknowledgements

First, I wish to express my sincere gratitude to my supervisor Dr. Md. Rafiqul Islam, Professor, Department of Electrical and Electronic Engineering, Khulna University of Engineering & Technology, Khulna, Bangladesh, for his invaluable support and excellent guidance. He has taught me not only a lot of technical work but also broadened my way of thinking and how to approach challenges.

I would like to thank Prof. Dr. Anisul Haque, Chairperson, Department of Electrical and Electronic Engineering, East West University, Dhaka, Bangladesh, for his valuable suggestions to complete this research works.

I am also grateful to Prof. Dr. Md. Nurunnabi Mollah and Dr. Md. Shahjahan for their valuable discussion on this work.

I would also like to thank Mr. Mohammad Shaifur Rahman, Mr. Mostafa Zaman Chowdhury and Mr. Md. Golam Kibria, faculty members of EEE, KUET, currently pursuing their higher studies in abroad, for their help in collecting important papers and books.

I also want to thank Dr. Md. Abdur Rafiq, Mr. Debabrata Kumar Karmokar, Mr. Md. Mohsin Ali, Mr. Khaled Mahbub Morshed, Mr. Md. Habibullah, and Mr. Md. Selim Hossain faculty members of KUET, for helping me during this research works especially in the time of my illness.

I must thank all the faculty members of EEE department, KUET for their help to complete the research works as a part-time student.

Abstracts

Strain-dependent and crystal orientation-dependent optical properties and output optical power-input current characteristics are numerically studied for GaInSb/GaInAlSb mid-infrared quantum well vertical cavity surface emitting laser (VCSEL). At first physical model of the VCSEL is proposed and then mathematical formulations is developed taking into account of strain, change in crystal orientation and piezoelectric field. The results obtained from the model are confirmed with the published results. To investigate the performances of the proposed VCSEL, wave functions, energy dispersion profiles, and momentum matrix elements are determined by Schrödinger equation using finite difference method. The results are calculated for a compressively strained quantum well in which strain is varied from 0.6% to 1.52% with the change in crystal orientation (001), (111), (110), (113), and (131). It is found that wave function confinement, energy separation between different bands and subbands, and magnitude of momentum matrix elements are strongly dependent on strain, change in crystal orientation and piezoelectric field. The injection carrier density-dependent optical and differential gains are calculated. Typical optical gains are found to be 3115, 3080, 2790, 3415, and 2940cm^{-1} in (001), (110), (111), (113), and (131) crystal orientations, respectively, when the injection carrier density is $3.5\times10^{18}\text{cm}^{-3}$. Further, the maximum differential gain is evaluated $2.78\times10^{-15}\text{cm}^2$ in (113) orientation for the injection carrier density $3.0\times10^{18}\text{cm}^{-3}$. The results obtained in the present study indicate that the peak emission wavelength can be tuned from 2.4μm to 2.25μm by changing crystal orientation from (110) to (111) in the well and barrier materials. It is also found that the influence of piezoelectric effect is not so remarkable on the optical gain and shift in peak emission wavelength for the proposed VCSEL.

To understand the output characteristics, the proposed VCSEL model is converted into PSPICE equivalent circuit. The results obtained from PSPICE simulation demonstrate that the maximum output power and the minimum threshold current are associated with the crystal orientation and the number of quantum wells. The highest optical power and lower threshold current are obtained when the crystal orientation is (113) and number of quantum well is three. Furthermore, design of distributed Bragg reflector indicates 30 and 38 pairs of alternating layer of $AlAs_{0.09}Sb_{0.91}$ and GaSb are used in top and bottom mirror in order to obtain reflectivity 99.13% and 99.8% reflectivity.

Contents

		PAGE
Title Page		i
Declaration		ii
Certificate of Research		iii
Acknowledgement		iv
Abstract		v
Contents		vi
List of Tables		viii
List of Figures		ix
List of Abbreviations		xi
CHAPTER 1	Introduction	1
	1.1 LASER Background	1
	1.2 Vertical Cavity Surface Emitting Lasers	2
	1.3 Mid-infrared Quantum Well VCSEL	3
	1.4 Present Status of Mid-infrared VCSELs Research	4
	1.5 Scope of The Thesis	5
	1.6 Layout of The Thesis	6
CHAPTER 2	Physical Structure and Mathematical Model	8
	2.1 Proposed QW VCSEL Structure	8
	2.2 Modeling of Electronic Energy Bands	9
	2.2.1 Conduction Band	9
	2.2.2 Valence Band	11
	2.2.3 Orientation-dependent Energy Band	15
	2.2.4 Energy Band Change due to Piezoelectric Field	17
	2.3 Optical Gain	18
	2.4 PSPICE Circuit Model	20
	2.5 DBR Design	26
	2.6 Model Verification	28
CHAPTER 3	Simulation Results and Discussion	35
	3.1 Band Structure and Gain in (001) Crystal Orientation.	37
	3.2 Band Structures and Optical Gain in (hkl) Orientation.	44
	3.3 Energy Bands Shift Due to Piezoelectric Field.	51
	3.4 Output Characteristics	53

CHAPTER 4	Concluding Remarks	58
	4.1 Conclusion	58
	4.2 Suggestion for Future Work	61
References		63
List of Publications on this dissertations		69

LIST OF TABLES

Table No.	Description	Page
2.6.1	The values of material parameters used for calculation of optical gain in $In_{0.65}Al_{0.20}Ga_{0.15}As/In_{0.36}Al_{0.24}Ga_{0.15}AS$ QW VCSEL. The parameters are calculated from the parameters of binary materials GaAs, InAs, and AlAs by interpolation. The parameters of binary materials are taken from the ref. [41].	29
2.6.2	The parameters used for calculation of gain in $Ga_{0.88}In_{0.12}As_{0.892}P_{0.108}/In_{0.49}Ga_{0.51}P$ QW VCSEL. The parameters are calculated from the parameters of binary materials GaAs, InP, InAs and GaP by interpolation. The parameters of binary materials are taken from the ref. [41].	31
2.6.3	The parameters used for the calculation of gain in (110) crystal orientated $In_{0.7}Ga_{0.3}As$ QW VCSEL. The parameters are calculated from the parameters of binary materials GaAs, InP, InAs, and GaP by interpolation. The parameters of binary materials are taken from the ref. [41].	33
3.1	Material parameters of GaSb, InSb and AlSb [41]. The material parameters of well and barrier are calculated from these binary parameters by interpolation.	36
3.3.1	Crystal orientation-dependent energy shifts due to piezoelectric fields for 0.9% strained QW.	52
3.2	Material parameterials used for evaulating output optical power characteristics. These parameters are calculated from the binary parameters of GaSb, InSb, AlSb and AsSb by interpolation. The binary parameters are taken from ref. [41].	54

LIST OF FIGURES

Figure No.	Description	Page
2.1	The physical structure of the proposed GaInSb QW VCSEL.	8
2.4.1	Carrier dynamics into the active region of the proposed VCSEL	20
2.4.2	PSPICE circuit model of a single differential equation.	23
2.4.3	Equivalent circuit model of two quantum well active regions.	25
2.5.1	Calculated mirror reflectivity for different number of $AlAs_{0.09}Sb_{0.91}/GaSb$ DBR pairs.	27
2.6.1	Comparison of normalized optical gain and PL intensity for $In_{0.65}Al_{0.20}Ga_{0.15}As/In_{0.36}Al_{0.24}Ga_{0.15}AS$ QW VCSEL. The PL intensity results are from ref. [37].	29
2.6.2:	Comparison of optical gain calculated by the proposed model with the result reported in the ref. [33].	30
2.6.3	Comparison of optical gain calculated by the proposed model in (110) orientation with the results reported in the ref. [29].	34
3.1.1	First conduction band (C1) wave function of $Ga_{0.65}In_{0.35}Sb$ QW estimated for different compressive strains.	38
3.1.2	Compressive strain-dependent conduction band (C1) dispersion profiles for $Ga_{0.65}In_{0.35}Sb$.	38
3.1.3	Compressive strain-dependent first heavy hole wave function of $Ga_{0.65}In_{0.35}Sb$ QW.	39
3.1.4	Compressive strain-dependent first light hole wave function of $Ga_{0.65}In_{0.35}Sb$ QW.	39
3.1.5	Compressive strain-dependent valence band dispersion profiles for $Ga_{0.65}In_{0.35}Sb$ quantum well.	40
3.1.6	Strain-dependent momentum matrix element squared for C1-HH1 transition.	41
3.1.7	Strain-dependent momentum matrix element squared for C1-LH1 transition.	42
3.1.8	Calculated optical gains of $Ga_{0.65}In_{0.35}Sb$ quantum well for different value of compressive strains	42
3.1.9	Peak gain as a function of carrier concentrations for different compressive strain QWs.	43
3.1.10	Differential gain with respect to injection carrier density for different compressive strained QW.	44

3.2.1	First heavy hole wave function of $Ga_{0.65}In_{0.35}Sb$ QW for different crystal orientations.	45
3.2.2	First light hole wave function of $Ga_{0.65}In_{0.35}Sb$ QW for different crystal orientations.	45
3.2.3	Valence band dispersion profiles of 0.9% compressive strained $Ga_{0.65}In_{0.35}Sb$ QW (a) (001), (b) (110), (c) (111), (d) (113), and (e) (131).	47
3.2.4	Orientation-dependent energy separations between the conduction and valence subbands for GaInSb strained QW.	47
3.2.5	Crystal orientation-dependent normalized momentum matrix element square for C1-HH1 transition.	48
3.2.6	Crystal orientation-dependent normalized momentum matrix element square for C1-LH1 transitions.	48
3.2.7	Optical gains evaluated in different crystal orientations for 0.9% compressive strained $Ga_{0.65}In_{0.35}Sb$ QW.	49
3.2.8	Carrier density-dependent optical gain in different crystal orientations for 0.9% compressive strained $Ga_{0.65}In_{0.35}Sb$ QW.	50
3.2.9	Differential gain with respect to injection carrier density in different orientations.	50
3.3.1	Effect of piezoelectric field on emission profile for 15nm 0.9% compressive strained $Ga_{0.65}In_{0.35}Sb$ quantum well in (131) crystal orientation.	51
3.3.2	Effect of piezoelectric field on emission profile for 15nm 1.52% compressive strained $Ga_{0.65}In_{0.35}Sb$ quantum well in (131) crystal orientation.	53
3.4.1.	Output optical power-input current characteristics of $Ga_{0.65}In_{0.35}Sb$ quantum well for different numbers of QWs.	55
3.4.2	Optical power characteristics of $Ga_{0.65}In_{0.35}Sb$ quantum well for different value of strain when number of QW is three.	56
3.4.3.	Output optical power-input current characteristics of 0.9% compressive strained $Ga_{0.65}In_{0.35}Sb$ QW for different crystal orientations.	57

List of abbreviations	
Abbreviated form	**Full meaning**
VCSEL	Vertical cavity surface emitting laser
QW	Quantum well
q-2D	Quasi-two-dimensional state of carrier
SCH	Separate confinement hetero-structure
DBR	Distributed Bragg Reflectors
QCSE	Quantum confined stark effect
PL	Photoluminescence
C	Conduction band
HH	Heavy hole
LH	Light hole

CHAPTER 1

Introduction

1.1 LASER Background

LASER is an acronym for Light Amplification by Stimulated Emission of Radiation. The laser makes use of processes that increase or amplify light signals. These processes include (1) stimulated emission, and (2) optical feedback that is usually provided by mirrors. Thus in its simplest form, a laser consists of a gain or amplifying medium and a set of mirrors to feed the light back into the amplifier for continued growth of developing beam [1].

Townes and Schawlow introduced the concept of laser by extending the maser operating frequency to optical range [2]. Maser is a microwave amplifier which produces a coherent beam of microwaves. Townes and Schawlow both received Noble prizes for their work in this field. In 1960, Theodore Maiman of Hughes Research Laboratories produced the first laser using ruby crystal as the amplifier and a flash lamp as the energy source [3]. The first gas laser was developed in 1961 by A. Javan, W. Bennett, and D. Harriott of Bell Laboratories, using a mixture of helium and neon gases [4]. At the same Laboratories, L.F. Jonson et al demonstrated the first neodymium laser, which has since become one of the most reliable lasers available [5]. The first semiconductor laser was demonstrated by R. Hall at General Electric Research Laboratories in 1962 [6]. The early semiconductor laser was based on p-n homojunction structure. But the carrier and optical confinement level in homojunction structure is not satisfactory. Again, homojunction laser cannot be operated continuously at room temperature which is a major drawback [7]. The carrier and optical confinement can be effectively achieved by double heterostructure. If the

active medium of double heterostructure is made thin then it is called quantum well. Lower threshold current and higher optical gain are the main performance parameters of a laser, that can be achieved by quantum well structure. In 1975, the first quantum well laser was made in a gallium arsenide semiconductor by J. van der Ziel and co-workers at Bell Laboratories [8]. After different structures of quantum well lasers were proposed which are mainly edge emitting and vertical cavity surface emitting quantum well lasers. In this thesis work, mid-infraed GaInSb quantum well vertical cavity surface emitting laser is proposed and its theoretical performances are studied.

1.2 Vertical Cavity Surface Emitting Lasers

Vertical cavity surface emitting lasers (VCSELs) are made by sandwiching light emitting layers (i.e., a thin semiconductor of high optical gain such as quantum wells) between two highly reflective mirrors. The mirrors can be dielectric multilayered or epitaxially grown mirrors working on the principle of distributed Bragg reflectors (DBRs). Light is taken out normally from the surfaces of the mirrors in VCSEL structures that enable coupling of emitted light sufficiently. The VCSEL family has several advantageous features over edge emitting lasers. In VCSELS, the separation between longitudinal modes is larger comparing to conventional edge emitting laser due to it much shorter cavity length and thus reduce mode hopping and chirp. It provides wafer testing facilities prior to packing. The manufacturing cost of VCSELs is much lower than conventional edge emitting lasers. It is possible to reduce the threshold current of VCSEL significantly due to recent breakthrough in current confinement in the active region. Higher optical power can be obtained in VCSEL structures by using the array operation. Moreover, VCSELs are very much attractive

due to its small size, excellent spectral properties, circular beam pattern, and low power consumption [7].

Vertical cavity surface emitting lasers (VCSELs) was first proposed and fabricated by K. Iga and his colleagues at the Tokyo Institute of Technology, Japan in the late 1970s [8]. They successfully demonstrated the first electrically pumped InGaAsP/InP VCSEL under pulse operation at 77 K in 1979 [9]. VCSEL oscillating at 980nm was developed on GaAs substrate [10]. Long wave length (above 1.3μm) VCSEL is generally grown on InP substrate [11]. The optical and electrical properties of long wavelength VCSEL have been imporved by using different ways. Among the ways polarization control by changing crystal orientations gives excelent PL intensity and voltage-current characteristics [12].

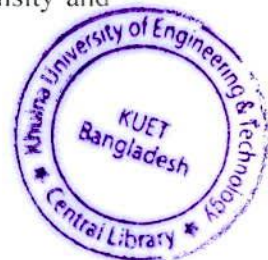
Khulna University of Engineering & Technology
KUET
Bangladesh
Central Library

1.3 Mid-infrared Quantum Well VCSEL

During the last few years Mid-infrared lasers (2~4μm) based on III–V compound semiconductors have become very much interesting due to its potential features. The strong correlation between the mid-infrared light absorption and glucose concentrations has made this window promising for non-invasive optical blood glucose monitoring through the skin [13]. In healthcare, mid-infrared lasers are also useful in breath analysis and imaging biological tissue [14, 15]. The CO sensing is an important task as it is a key indicator of combustion efficiency and it also plays a vital role in air pollution. The mid-infrared light sources can be used in detecting CO as reported so far [16]. It is well known that, Light sources oscillating in Mid-infrared wavelength can also be used in chemical sensing by using absorption spectroscopy [17]. The reduced scattering and higher throughput properties of mid-infrared light sources recently has drawn keen research interest to use it in free space optical

communication, particularly, in adverse weather condition like fog [18]. Due to reduced optical loss in fluoride and sapphire glass fiber [19, 20], it is suggested to use mid-infrared lasers for future optical fiber communication system.

1.4 Present Status of Mid-infrared VCSELs Research

Extensive researches have already been carried out experimentally and theoretically to investigate the optical and electrical properties of 1.3μm and 1.55μm VCSELs. Compared with the research on 1.3μm and 1.55μm VCSELs, mid-infrared VCSELs is immature. Research works on mid-infrared VCSEL are of immense important, because of its wide range of applications in different fields.

The first mid-infrared laser was demonstrated from lead-based IV-VI semiconductors [21]. But, the Pb-salts lasers developed have been shown to be problematic in achieving high power, high efficiency, high reliability and output power is typically lower than 1mW. Electrically pumped GaInAsSb double heterostructure laser was first realized in 1986 by Caneau et al [22]. To reduce the threshold current of double heterostructure, QW structure is used as gain medium. In QW structure, GaInAsSb/ AlGaAsSb material is also used in active region [23, 24]. But, the miscibility gap of quaternary InGaAsSb QW material limits the range of stable compositions and often tends to segregate into inhomogeneous mixtures of binaries and ternaries at equilibrium temperature [25]. Type-II GaInSb/InAs material system is also used in the well of active region for mid-infrared photonic applications [26]. But, Type-II GaInSb/InAs superlattice has inherent problem of large recombination time due to its electron and hole confinement in different layers [27]. On the other hand, GaInSb is a ternary material, which is comparatively easy to grow with high quality and homogenous composition. Again, the recombination time in GaInSb/GaInAlSb quantum well is comparatively lower due to its electron and hole localization in same

region of space. To avoid the structural degradation associated with the miscibility gap and efficient recombination, GaInSb/GaInAlSb material system is better for mid-infrared lasers. Furthermore; GaInSb/GaInAlSb material system offers an excellent compromise between the requirements for good electronic and optical confinement as well as low series resistance in the laser structure. The temperature-dependent properties of most important GaInSb/ GaInAlSb quantum well structures have been experimentally demonstrated using electroluminescence experiment by G.R. Nash et al [28, 29]. To best of our knowledge, there are no theoretical as well as experimental studies on the emission properties of GaInSb/ GaInAlSb VCSELs on account of strains, crystal orientations, temperature and piezoelectric fields. It is therefore very much important to develop a suitable model for GaInSb/GaInAlSb QW mid-infrared VCSEL and then to investigate its various performances in order to optimize experimental parameters and hence to reduce the cost and complexity of the experiments.

1.5 Scope of The Thesis

The main objective of this thesis is to propose a model for GaSb-based QW VCSEL considering the effect of strain, change in crystal orientations and piezoelectric field. To investigate the emission properties of the proposed VCSEL, it is necessary to determine the conduction and valence band wave functions, eignenergies of the proposed VCSEL. The conduction and valence energy bands are calculated by solving the Schrödinger equation for the proposed VCSEL using finite difference method. The wave functions and eignenergies of the proposed QW VCSEL are calculated considering strain, crystal orientations, and piezoelectric fields. The emission profiles of the proposed VCSEL are analyzed with the facts discussed above. The carrier-density dependent optical gain is calculated for the proposed VCSEL. The physical

structure of the laser is converted into the PSPICE equivalent circuit using the laser rate equations to determine the optical output power-injection current characteristics. The optical output power-injection current characteristics are evaluated using the equivalent circuit for different strain values and crystal orientations. DBR is also an important part for the proposed VCSEL. Here, multilayered suitable materials are proposed so that desired reflectivity can be obtained with less no. of DBR pairs. The reflectivity of DBR is also calculated considering refractive index and energy band gap of the materials.

1.6 Layout of The Thesis

This dissertation describes the modeling and performances analysis of mid-infrared VCSEL. The research work is divided into several chapters in which device design, mathematical modeling, device performances and output characteristics are discussed. In chapter 1 background of the present work is explained. Present status and future prospect of the present work are described clearly in this chapter. Finally objectives of the present work are also summarized in this chapter.

Chapter 2 starts with a description of physical structure of the proposed QW VCSEL. The mathematical modeling of the proposed device has been presented in this chapter. The mathematical modeling consists of finite difference solution technique of Schrödinger equation, orientation-dependent and piezoelectric field dependent energy band calculation, PSPICE circuit simulation, and DBR design. Schrödinger equation is solved considering the effect strain and change in crystal orientation. The procedures of converting the physical structure into equivalent circuit model and analysis technique have been discussed in this chapter. This chapter also contains the verifications of the proposed model with published results.

In chapter 3, the results obtained based on mathematical modeling of the proposed laser structure are presented. The effect of stain and change in crystal orientation on conduction and valence bands and gain profiles are the main concern of this chapter. The effect of piezoelectric fields on energy band and optical gain are presented here. The output optical power-input current characteristics of the proposed VCSEL are also shown for different values of strain and crystal orientations.

Chapter 4 provides the conclusion of the present research and the prospect for the future studies.

CHAPTER 2

Physical Structure and Mathematical Model

This section describes the physical structure and mathematical model of strain and crystal orientation dependent electrical and optical properties of mid-infrared quantum well VCSEL. In order to analyze electronic band structure, one dimensional Schrödinger equations for conduction and valence bands are solved by finite difference method. A suitable DBR is designed and PSPICE equivalent circuit model is developed for the proposed VCSEL structure. The validity of the proposed model is also explained in this chapter.

2.1 Proposed QW VCSEL Structure

The physical structure of (001) and arbitrary crystal orientated (hkl) QW VCSEL is shown in fig.2.1. Here 7nm GaInSb quantum well is sandwiched between 7nm GaInAlSb barrier layers. The well layer is compressively strained due to lattice mismatched between well and cladding layers. A high band gap GaInAsSb layer is used as cladding layer which is lattice matched to the barrier layer. Two lattice-matched $AlAs_{0.09}Sb_{0.91}$/GaSb DBRs of mean reflectivity 99.5% are also used as mirrors. All the layers are grown on GaSb substrate. In arbitrary crystal orientated VCSEL structure, the

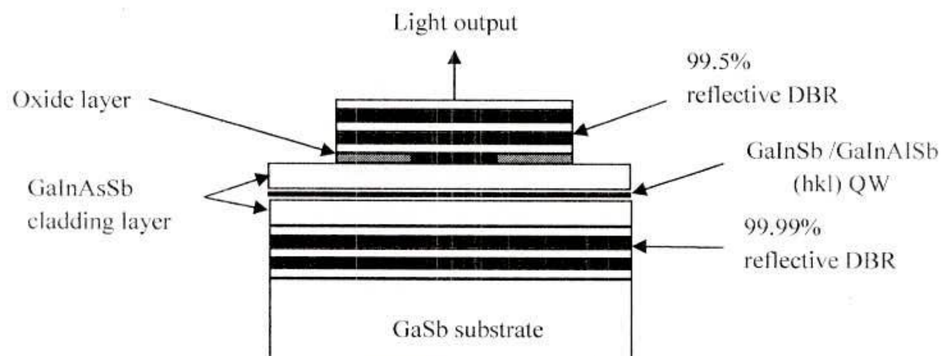

Fig.2.1 The physical structure of the proposed GaInSb QW

crystal orientation in the active region (well, barrier and cladding layer) is changed arbitrarily but the two DBRs and substrate are in (001) crystal orientation as it is hard to grow high quality bulk material in (hkl) orientation [28]. The interface of (001) or (hkl) orientation can be joined by wafer bonding technique. Here, the stain the active region is determined by the lattice mismatched between the well and cladding materials as the width of cladding layer is higher than the barrier layer.

2.2 Modeling of Electronic Energy Bands

To understand the optical properties of the proposed VCSEL, we have to know the electronic energy bands dispersion profiles and their wave functions. Strain, crystal orientations and piezoelectric field are the key parameters that can modify the electronic band structure. Mathematical formulations of energy band structure including the effect of strain, change in crystal orientations and piezoelectric field are given below.

2.2.1 Conduction Band

Conduction band dispersion profile is assumed to be parabolic in our calculation. One dimension Schrödinger equation is used for finding discrete energy levels of QW VCSEL [30]. The one dimension Schrödinger equation for conduction band is given below:

$$\left[\frac{-\hbar^2}{2m^*_e}\frac{d^2}{dz^2}+v_e(z)\right]\psi_n(z)=E_e(k_t=0)\psi_n(z) \tag{1}$$

where $\psi_n(z)$ conduction band wave function, $\hbar$ Planck's constant divided by 2π, m_e^* effective mass of the electron, E_e electron energy level, k_t inplane wave vector, and $v_e(z)$ is the conduction band potential which can be given by [30]

$$v_e = \begin{cases} a_c(\varepsilon_{11} + \varepsilon_{22} + \varepsilon_{33}) & |z| \le \frac{L_w}{2} \\ \Delta v_e & |z| \ge \frac{L_w}{2} \end{cases} \tag{2}$$

where, L_w is the QW length, a_c is the conduction band deformation potential, $\varepsilon_{11}, \varepsilon_{22}, and\ \varepsilon_{33}$ are the principal strain component in (100), (010) and (001) directions respectively, Δv_e is the conduction band offset in barrier layer.

Finite difference discretization of equation (1) is

$$\frac{-h^2}{2m_e^*}\left(\frac{\psi_{i+1} - 2\psi_i + \psi_{i-1}}{\Delta z^2}\right) + v_i\psi_i = E_e(k_t = 0)\psi_i \tag{3}$$

In our analysis, total active region L is divided into number of sections for computational purpose. If the number of node is N, then spacing between nodes is determined by, $\Delta z = L/(N-1)$. The boundary condition in the present study is $\psi(z) = 0$ for outside the well and barrier regions. The index i can be varied from $i = 1$ to $i = N-1$. Equation (3) can be written as

$$\frac{-\hbar^2}{2m_c^*\Delta z^2}[\psi_2 - 2\psi_1 + \psi_0] + v_1\psi_1 = E_e\psi_1 \tag{4}$$

$$\frac{-\hbar^2}{2m_e^*\Delta z^2}[\psi_3 - 2\psi_2 + \psi_1] + v_2\psi_2 = E_e\psi_2, \tag{5}$$

and

$$\frac{-\hbar^2}{2m_e^*\Delta z^2}[\psi_N - 2\psi_{N-1} + \psi_{N-2}] + v_{N-1}\psi_{N-1} = E_e\psi_{N-1} \tag{6}$$

for $i = 1,2,....(N-1)$, respectively. Outside the well and barrier regions the wave functions ψ_0 and ψ_N are equal to zero. The resulting Hamiltonian matrix in the present case can be given by

$$H_c = \frac{-\hbar^2}{2m^*_e \Delta z^2}\begin{bmatrix} -2 & 1 & 0 & 0 & 0 & 0 & 0 \\ 1 & -2 & 1 & 0 & 0 & 0 & 0 \\ 0 & 1 & -2 & 1 & 0 & 0 & 0 \\ 0 & 0 & 1 & -2 & 1 & 0 & 0 \\ 0 & 0 & 0 & 1 & -2 & 1 & 0 \\ 0 & 0 & 0 & 0 & 1 & -2 & 1 \\ 0 & 0 & 0 & 0 & 0 & 1 & -2 \end{bmatrix} + \begin{bmatrix} v_1 & 0 & 0 & 0 & 0 & 0 & 0 \\ 0 & v_2 & 0 & 0 & 0 & 0 & 0 \\ 0 & 0 & v_3 & 0 & 0 & 0 & 0 \\ 0 & 0 & 0 & v_4 & 0 & 0 & 0 \\ 0 & 0 & 0 & 0 & v_5 & 0 & 0 \\ 0 & 0 & 0 & 0 & 0 & v_6 & 0 \\ 0 & 0 & 0 & 0 & 0 & 0 & v_{N-1} \end{bmatrix} \tag{7}$$

Conduction band energies and corresponding wave vectors are evaluated by finding the eign-values and eign-vectors of the Hamiltonian matrix. The conduction band energy dispersion relation can be written as [31].

$$E(k_t) = E(k_t = 0) + \frac{\hbar^2 k_t^{\ 2}}{2m_e^{\ *}} \tag{8}$$

where $k_t^{\ 2} = k_1^{\ 2} + k_2^{\ 2}$

Here, k_1 and k_2 are the wave vectors at (100) and (010) directions.

2.2.2 Valence Band

For valence band, we start with effective-mass theory on quantum wells using the Luttinger-Kohn 4×4 Hamiltonian matrix including the effect of biaxial strain. The Luttinger-Kohn 4×4 Hamiltonian matrix can be expressed by [31]

$$H\psi_h(z) = E\psi_h \tag{9}$$

where H is resultant Hamiltonian matrix that can be given by

$$H = H_0 + H_\varepsilon \tag{10}$$

The components of resultant Hamiltonian matrix are given below

$$H_0 = \begin{bmatrix} H_{hh} & b & c & 0 \\ b^* & H_{lh} & 0 & c \\ c^* & 0 & H_{lh} & -b \\ 0 & c^* & -b^* & H_{hh} \end{bmatrix} \tag{11}$$

and

$$\psi_h(z) = \begin{bmatrix} \phi_{3/2,3/2}(z) \\ \phi_{3/2,1/2}(z) \\ \phi_{3/2,-1/2}(z) \\ \phi_{3/2,-3/2}(z) \end{bmatrix} = \begin{bmatrix} g^{(1)}(z) \\ g^{(2)}(z) \\ g^{(3)}(z) \\ g^{(4)}(z) \end{bmatrix} \tag{12}$$

ϕ_{j,m_j} or $g^{(j)}$ is the valence band wave function component and E is the energy of heavy and light holes. The matrix elements H_{hh}, H_{lh}, b and c are:

$$H_{hh} = \left\{ \frac{-\hbar^2}{2m_0} \left[(\gamma_1 + \gamma_2)k_t^2 - (\gamma_1 - 2\gamma_2)\frac{\partial^2}{\partial z^2} \right] + v(z) \right\},$$

$$H_{lh} = \left\{ \frac{-\hbar^2}{2m_0} \left[(\gamma_1 - \gamma_2)k_t^2 - (\gamma_1 + 2\gamma_2)\frac{\partial^2}{\partial z^2} \right] + v(z) \right\},$$

$$b = \frac{i\sqrt{3}\hbar^2}{m_0}(-k_2 - ik_1)\gamma_3 \frac{\partial}{\partial z}$$

and

$$c = -\frac{\sqrt{3}\hbar^2}{2m_0}\left[\gamma_2(k_1^2 - k_2^2) - 2i\gamma_3 k_1 k_2\right] \tag{13}$$

where m_0 is the free electron mass, γ_1, γ_2 and γ_3 are the Luttinger parameters, k_1 and k_2 are the components of transverse wave vector and $k_t^2 = k_1^2 + k_2^2$. The potential profile of the valence band, $v_h(z)$ is

$$v_h = \begin{vmatrix} 0 & |z| \le \frac{L_w}{2} \\ \Delta v_h & |z| \ge \frac{L_w}{2} \end{vmatrix} \tag{14}$$

Δv_h is the valence band offset for the barrier layer. According to the finite difference method, equation (13) can be represented by

$$H_{hh}\phi_{j,m_j}(z) = \left\{ \frac{-\hbar^2}{2m_0} \left[(\gamma_1 + \gamma_2)k_t^{\ 2} - (\gamma_1 - 2\gamma_2)\frac{\partial^2}{\partial z^2} \right] + v(z) \right\} \phi_{j,m_j}(z)$$

$$= \left\{ \frac{-\hbar^2}{2m_0} \left[(\gamma_1 + \gamma_2)k_t^{\ 2} - (\gamma_1 - 2\gamma_2)\frac{-2}{\Delta z^2} \right] + v(z_i) \right\} \phi_{j,m_j}(z_i)$$

$$+ \left\{ \frac{-\hbar^2}{2m_0} \left[-(\gamma_1 - 2\gamma_2)\frac{1}{\Delta z^2} \right] \right\} \phi_{j,m_j}(z_{i+1}) + \left\{ \frac{-\hbar^2}{2m_0} \left[-(\gamma_1 - 2\gamma_2)\frac{1}{\Delta z^2} \right] \right\} \phi_{j,m_j}(z_{i-1})$$

$$= f\phi_{j,m_j}(z_{i+1}) + e_i\phi_{j,m_j}(z_i) + f\phi_{j,m_j}(z_{i-1}) \tag{15}$$

$$H_{lh}\phi_{j,m_j}(z) = \left\{ \frac{-\hbar^2}{2m_0} \left[(\gamma_1 - \gamma_2)k_t^{\ 2} - (\gamma_1 + 2\gamma_2)\frac{\partial^2}{\partial z^2} \right] + v(z) \right\} \phi_{j,m_j}(z)$$

$$= \left\{ \frac{-\hbar^2}{2m_0} \left[(\gamma_1 - \gamma_2)k_t^{\ 2} - (\gamma_1 + 2\gamma_2)\frac{-2}{\Delta z^2} \right] + v(z_i) \right\} \phi_{j,m_j}(z_i)$$

$$+ \left\{ \frac{-\hbar^2}{2m_0} \left[-(\gamma_1 + 2\gamma_2)\frac{1}{\Delta z^2} \right] \right\} \phi_{j,m_j}(z_{i+1}) + \left\{ \frac{-\hbar^2}{2m_0} \left[-(\gamma_1 + 2\gamma_2)\frac{1}{\Delta z^2} \right] \right\} \phi_{j,m_j}(z_{i-1})$$

$$= f'\phi_{j,m_j}(z_{i+1}) + e_i'\phi_{j,m_j}(z_i) + f'\phi_{j,m_j}(z_{i-1}) \tag{16}$$

$$b\phi_{j,m_j}(z_i) = \frac{i\sqrt{3}\hbar^2}{m_0}(-k_2 - ik_1)\gamma_3 \frac{\partial}{\partial z}\phi_{j,m_j}(z_i)$$

$$= \frac{i\sqrt{3}\hbar^2}{m_0}(-k_2 - ik_1)\gamma_3 \left(\frac{\phi_{j,m_j}(z_{i+1}) - \phi_{j,m_j}(z_{i-1})}{2\Delta z} \right)$$

$$= \beta\phi_{j,m_j}(z_{i+1}) - \beta\phi_{j,m_j}(z_{i-1}) \tag{17}$$

and

$$c\phi_{j,m_j}(z_i) = -\frac{\sqrt{3}\hbar^2}{2m_0}\left[\gamma_2(k_1^{\ 2} - k_2^{\ 2}) - 2i\gamma_3 k_1 k_2 \right] \phi_{j,m_j}(z_i) \tag{18}$$

where,

$$e_i = \frac{-\hbar^2}{2m_0}\left[(\gamma_1+\gamma_2)k_t^{\,2} - (\gamma_1 - 2\gamma_2)\frac{-2}{\Delta z^2}\right] + v(z_i)$$
$$e_i' = \frac{-\hbar^2}{2m_0}\left[(\gamma_1-\gamma_2)k_t^{\,2} - (\gamma_1 + 2\gamma_2)\frac{-2}{\Delta z^2}\right] + v(z_i)$$
$$f = \frac{-\hbar^2}{2m_0}\left[-(\gamma_1 - 2\gamma_2)\frac{1}{\Delta z^2}\right]$$
$$f' = \frac{-\hbar^2}{2m_0}\left[-(\gamma_1 - 2\gamma_2)\frac{1}{\Delta z^2}\right]$$

Khulna University of Engineering & Technology
KUET
Bangladesh
Central Library

and

$$\beta = \frac{i\sqrt{3}\hbar^2}{m_0}(-k_2 - ik_1)\gamma_3\left(\frac{1}{2\Delta z}\right) \tag{19}$$

Putting $i = 1,2,...(N-1)$ in equation (15-19), and then substitute them into equation (11), we obtained the desired Hamiltonian matrix. The Hamiltonian matrix calculated as an example for $N = 4$. Here hole wave functions outside the well and barrier regions are set to zero, i.e. $\psi_h(z_0) = \psi_h(z_4) = 0$. In this model Luttinger parameters are space-dependent (in well region it well be the parameters of well material and barrier region it will the paramters of barrier).

$$\begin{array}{cccccccccccccc}
 & \multicolumn{4}{c}{\text{Node 1}} & \multicolumn{4}{c}{\text{Node 2}} & \multicolumn{4}{c}{\text{Node 3}} \\
 & 3/2 & 1/2 & -1/2 & -3/2 & 3/2 & 1/2 & -1/2 & -3/2 & 3/2 & 1/2 & -1/2 & -3/2
\end{array}$$

$$H_0 = \begin{bmatrix}
e_1 & 0 & c_1 & 0 & f_2 & \beta_2 & 0 & 0 & 0 & 0 & 0 & 0 \\
0 & e_1' & 0 & c_1 & \beta_2^{*} & f'_2 & 0 & 0 & 0 & 0 & 0 & 0 \\
c_1^{*} & 0 & e_1' & 0 & 0 & 0 & f'_2 & -\beta_2 & 0 & 0 & 0 & 0 \\
0 & c_1^{*} & 0 & e_1 & 0 & 0 & -\beta^{*}{}_2 & f_2 & 0 & 0 & 0 & 0 \\
f_1 & -\beta_1 & 0 & 0 & e_2 & 0 & c & 0 & f_3 & \beta_3 & 0 & 0 \\
-\beta_1^{*} & f_1' & 0 & 0 & 0 & e_2' & 0 & c_2 & \beta_3^{*} & f'_3 & 0 & 0 \\
0 & 0 & f'_1 & \beta_1 & c^{*} & 0 & e_2' & 0 & 0 & 0 & f'_3 & -\beta_3 \\
0 & 0 & \beta^{*}{}_1 & f_1 & 0 & c^{*}{}_2 & 0 & e_2 & 0 & 0 & -\beta^{*}{}_3 & f_3 \\
0 & 0 & 0 & 0 & f_2 & -\beta_2 & 0 & 0 & e_3 & 0 & c_3 & 0 \\
0 & 0 & 0 & 0 & -\beta^{*}{}_2 & f'_2 & 0 & 0 & 0 & e_3' & 0 & c \\
0 & 0 & 0 & 0 & 0 & 0 & f'_2 & \beta_2 & c_3^{*} & 0 & e_3' & 0 \\
0 & 0 & 0 & 0 & 0 & 0 & \beta^{*}{}_2 & f_2 & 0 & c_3^{*} & 0 & e_3
\end{bmatrix} \tag{20}$$

The other element of the resultant Hamiltonian matrix, H_ε shown in equation (10) is the strain Hamiltonian matrix and can be given by [12]

$$H_\varepsilon = \begin{bmatrix} A & -S_\varepsilon & R_\varepsilon & 0 \\ -S_\varepsilon^* & -A & 0 & R_\varepsilon \\ R_\varepsilon^* & 0 & -A & S_\varepsilon \\ 0 & R_\varepsilon^* & S_\varepsilon^* & A \end{bmatrix} + (a_v)(\varepsilon_{11}+\varepsilon_{22}+\varepsilon_{33})I_4 \tag{21}$$

The components of H_ε matrix are:

$$\begin{aligned} A &= -\frac{1}{2}b(\varepsilon_{11}+\varepsilon_{22}-2\varepsilon_{33}) \\ R_\varepsilon &= \frac{1}{2}\left[\sqrt{3}b(\varepsilon_{11}-\varepsilon_{22})-id\varepsilon_{12}\right] \\ S_\varepsilon &= -\sqrt{3}d(\varepsilon_{13}-i\varepsilon_{23}) \end{aligned} \tag{22}$$

Here, a_v is the valence band deformation potential, b and d are the shear deformation potentials, I_4 is the unit matrix. To obtain the total Hamiltonian matrix it is necessary to calculate the strain Hamiltonian matrix at different nodes. Here, an example of Hamiltonian matrix is presented for $N = 4$

	Node 1				Node 2				Node 3			
	3/2	1/2	-1/2	-3/2	3/2	1/2	-1/2	-3/2	3/2	1/2	-1/2	-3/2

$$H_\varepsilon = \begin{bmatrix}
A(z_1) & -S_\varepsilon(z_1) & R_\varepsilon(z_1) & 0 & 0 & 0 & 0 & 0 & 0 & 0 & 0 & 0 \\
-S_\varepsilon^*(z_1) & -A(z_1) & 0 & R_\varepsilon(z_1) & 0 & 0 & 0 & 0 & 0 & 0 & 0 & 0 \\
R_\varepsilon^*(z_1) & 0 & -A(z_1) & S_\varepsilon(z_1) & 0 & 0 & 0 & 0 & 0 & 0 & 0 & 0 \\
0 & R_\varepsilon^*(z_1) & S_\varepsilon^*(z_1) & A(z_1) & 0 & 0 & 0 & 0 & 0 & 0 & 0 & 0 \\
0 & 0 & 0 & 0 & A(z_2) & -S_\varepsilon(z_2) & R_\varepsilon(z_2) & 0 & 0 & 0 & 0 & 0 \\
0 & 0 & 0 & 0 & -S_\varepsilon^*(z_2) & -A(z_2) & 0 & R_\varepsilon(z_2) & 0 & 0 & 0 & 0 \\
0 & 0 & 0 & 0 & R_\varepsilon^*(z_2) & 0 & -A(z_2) & S_\varepsilon(z_2) & 0 & 0 & 0 & 0 \\
0 & 0 & 0 & 0 & 0 & R_\varepsilon^*(z_2) & S_\varepsilon^*(z_2) & A(z_2) & 0 & 0 & 0 & 0 \\
0 & 0 & 0 & 0 & 0 & 0 & 0 & 0 & A(z_3) & -S_\varepsilon(z_3) & R_\varepsilon(z_3) & 0 \\
0 & 0 & 0 & 0 & 0 & 0 & 0 & 0 & -S_\varepsilon^*(z_3) & -A(z_3) & 0 & R_\varepsilon(z_3) \\
0 & 0 & 0 & 0 & 0 & 0 & 0 & 0 & R_\varepsilon^*(z_3) & 0 & -A(z_3) & S_\varepsilon(z_3) \\
0 & 0 & 0 & 0 & 0 & 0 & 0 & 0 & 0 & R_\varepsilon^*(z_3) & S_\varepsilon^*(z_3) & A(z_3)
\end{bmatrix}$$
$$+(a_v)(\varepsilon_{11}+\varepsilon_{22}+\varepsilon_{33})I_{16} \tag{23}$$

From the resultant Hamiltonian matrix H, the eignenergy and eignvectors of $\phi_{3/2,3/2}$ and $\phi_{3/2,1/2}$ are calculated and then dispersion profiles are obtained as a function of wave vector. The eignenergy and eignvectors of $\phi_{3/2,3/2}$ and $\phi_{3/2,1/2}$ are the energy and wavefunction of heavy and light respectively.

2.2.3 Orientation-dependent Energy Band

As the conduction band wave function does not change with crystal orientation, here we are interested about the modification in the valence band Hamiltonian matrix owing to crystal orientations [12]. If the active region is grown on arbitrary crystal orientation (hkl), the wave vectors on (001) crystal can be obtained by the following expression [32]

$$\begin{pmatrix} k_1 \\ k_2 \\ k_3 \end{pmatrix} = O_R \begin{pmatrix} k_x \\ k_y \\ k_z \end{pmatrix} \tag{24}$$

where, k_x, k_y, k_z are the wave vectors along (hkl) direction.

and the strain on (001) crystal orientation can be calculated by [32]

$$\begin{pmatrix} \varepsilon_{11} & \varepsilon_{12} & \varepsilon_{13} \\ \varepsilon_{21} & \varepsilon_{22} & \varepsilon_{23} \\ \varepsilon_{31} & \varepsilon_{32} & \varepsilon_{33} \end{pmatrix} = O_R \begin{pmatrix} \varepsilon_{xx} & \varepsilon_{xy} & \varepsilon_{xz} \\ \varepsilon_{yx} & \varepsilon_{yy} & \varepsilon_{xz} \\ \varepsilon_{zx} & \varepsilon_{zy} & \varepsilon_{zz} \end{pmatrix} O_R^{\ T} \tag{25}$$

Here, $\varepsilon_{ij}(i, j = x, y, z)$ are the strain tensors in (hkl) direction. Since the barrier layer is very thin (7nm) comparing to the cladding layer (500nm), the strain is calculated considering the lattice mismatch between well and cladding layers. The values of diagonal elements are

$$\varepsilon_{xx} = \varepsilon_{yy} = \varepsilon_{II} = (a_{well} - a_{cld}) / a_{cld} \tag{26}$$

$$\varepsilon_{zz} = -\frac{C_{11}}{2C_{12}} \varepsilon_{II} \tag{27}$$

Here, C_{11} and C_{12} are the elastic constants of the well material, a_{well} and a_{cld} are the lattice constant of well and cladding layer respectively. The values of off-diagonal matrix element are set to zero incase of in-plane strain condition.

The expression of the rotation matrix is as follows [32]

$$O_R = \begin{pmatrix} \cos\theta\cos\phi & -\sin\phi & \sin\theta\cos\phi \\ \cos\theta\sin\phi & \cos\phi & \sin\theta\sin\phi \\ -\sin\theta & 0 & \cos\theta \end{pmatrix} \tag{28}$$

where, $\theta = \tan^{-1}(\frac{\sqrt{(h^2+k^2)}}{l})$ and $\phi = \tan^{-1}(k/h)$ (29)

Using the wave vector and strains in the (001) crystal orientation, the Hamiltonian matrix for (001) crystal orientation can be calculated according to section 2.2.2. Then the Hamiltonian matrix in (hkl) orientation can be calculated by the following equation for both well and barrier regions [33]

$$H^{hkl} = UH^{(001)}U^* \tag{30}$$

where $U = R(\theta)R(\phi)$ (31)

Here, $R(\theta)$ and $R(\phi)$ represent the spinor rotations which transform the (001) orientated valence band Hamiltonian to arbitrary crystal orientated Hamiltonian matrix. The expression of $R(\theta)$ and $R(\phi)$ can be given by [33]

$$R(\theta) = \begin{pmatrix} \alpha^2 & -\sqrt{3}\alpha^2\zeta & \sqrt{3}\alpha\zeta^2 & \zeta^3 \\ \sqrt{3}\alpha^2\zeta & \alpha^3 - 2\alpha\zeta^2 & -2\alpha^2\zeta + \zeta^3 & \sqrt{3}\alpha\zeta^2 \\ \sqrt{3}\alpha\zeta^2 & 2\alpha^2\zeta - \zeta^3 & \alpha^3 - 2\alpha^2\zeta & -\sqrt{3}\alpha^2\zeta \\ \zeta^3 & \sqrt{3}\alpha\zeta^2 & \sqrt{3}\alpha^2\zeta & \alpha^3 \end{pmatrix} \tag{32}$$

Here

$$\alpha = \cos\frac{\theta}{2} \text{ and } \zeta = -\sin\frac{\theta}{2} \tag{33}$$

$$R(\phi) = \begin{pmatrix} e^{i(3/2)\phi} & 0 & 0 & 0 \\ 0 & e^{i(1/2)\phi} & 0 & 0 \\ 0 & 0 & e^{-i(1/2)\phi} & 0 \\ 0 & 0 & 0 & e^{-i(3/2)\phi} \end{pmatrix} \tag{34}$$

2.2.4 Energy Band Change Due to Piezoelectric Field

The piezo-electric field in the QW structure has orientation dependent characteristics. In case of cubic crystal, the piezo-electric field is zero in (001) orientation. But, in arbitrary orientation the effect of piezo-electric field is present. The piezoelectric polarization in the (100), (010) and (001) directions can be expressed by [34]

$$P_i = 2e_{14}\varepsilon_{jk} \tag{35}$$

Here, e_{14} is the piezoelectric constant for the material. The values of the index $i, j, k = 1,2,3$ and $i \neq j \neq k$.

The piezoelectric polarization along the (hkl) direction is [12]

$$\begin{bmatrix} P_x \\ P_y \\ P_z \end{bmatrix} = O_R^{\,T} \begin{bmatrix} P_1 \\ P_2 \\ P_3 \end{bmatrix} \tag{36}$$

The associated electric piezoelectric field in the z direction is

$$E_z = \frac{P_z}{\varepsilon_0 \varepsilon_r} \tag{37}$$

Here, ε_r relative dielectric constant of the material.

From the quantum confinement stark effect theory (QCSE), the energy shift due to piezoelectric field for quantum well structure can be given by [35].

$$\Delta E = C\frac{m^* e^2 E_z^{\,2} L^4}{\hbar^2} \quad ; C = \frac{1}{8}\left(\frac{1}{3} - \frac{2}{\pi^2}\right)^2 \tag{38}$$

where L = Quantum well length and m^* is the mass of electron or hole.

Then the energy band profiles are changed due to piezoelectric field can be given by [27]

$E_c = E_c(E_z = 0) + \Delta E^c$ and $E_p = E_p(E_z = 0) + \Delta E^h$ .Here, E_c and E_p are the energy of electron and hole respectively.

2.3 Optical Gain

The optical gain as a function of energy for quantum well structures can be expressed by [36]

$$g(E)=\frac{2q^2\hbar}{n\varepsilon_0 c m_0^2 LE}\times\sum_{n,m}\int_0^{\pi}\frac{k_t M_{nm}(k_t)\Gamma/(2\pi)}{(E_{cn}(k_t)-E_{kpm}(k_t)-E)^2+(\Gamma/2\pi)^2}(f_c^n-f_v^m)dk_t \tag{39}$$

where, q is the free electron charge, $\hbar$ is the reduced Planck constant, n is the index of refraction, ε_0 free space dielectric constant, c is the speed of light, E is the photon energy, E_{cn} is the n-th conduction subbands, E_{kpm} is the m-th valence subbands, and M_{nm} is the momentum matrix element in strained quantum well. $\Gamma=\frac{h}{\tau}$; τ is the photon relaxation time. Fermi functions for the conduction band and valence bands are [31]

$$f_c^n(k_t)=\frac{1}{1+\exp\{[E_c^n(k_t)+(m_r/m_e^*)(E-(E_{cn}(k_t)-E_{kpm}(k_t)))-F_c]/KT\}} \tag{40}$$

$$f_v^m(k_t)=\frac{1}{1+\exp\{[E_{kpm}(k_t)-(m_r/m_h^*)(E-(E_{cn}(k_t)-E_{kpm}(k_t)))-F_v]/KT\}} \tag{41}$$

where F_c, F_v are the quasi-fermi levels of conduction and valence bands. In carrier density-dependent quasi-fermi levels calculation, it is considered that the injected carrier is electron. The expressions of quasi-fermi levels can be given by [31]

$$F_c=E_{c1}(k_t=0)+KTln\left(\frac{N_{inj}+n_i}{N_c}\right) \tag{42}$$

$$F_v = E_{kp1}(k_t = 0) - KTln\left(\frac{N_{dop} + n_i}{N_v}\right) \quad (43)$$

where E_{c1} and E_{kp1} are the first conduction and valence band energy at band edge, N_{inj} is the injected carrier density, N_{dop} is the p-type doping density in the well, n_i is the intrinsic carrier density, N_c and N_v are the density of state of electron and hole for the QW material. Although the proposed structure is QW, here three dimensional density of state is considered as the injection carrier density is three dimensional.

Incase of compressive strained QW TE optical gain is dominating. The TE mode momentum matrix element for interband transition can be written as [31]

$$M_{nm}(k_t) = 2\frac{3}{4}\left[\left\langle \psi_{n(k_t=0)} \middle| g^{(1)}{}_m \right\rangle^2 + \frac{1}{3}\left\langle \psi_{n(k_t=0)} \middle| g^{(2)}{}_m \right\rangle^2\right] M_b{}^2 \quad (44)$$

where $\left\langle \psi_{n(k_t=0)} \middle| g^{(1)}{}_m \right\rangle = \int_{-\infty}^{\infty} \psi_{n(k_t=0)}(z) g^{(1)}{}_m(z) dz$, but in our proposed model, we integrate the wave functions in the well and barrier region. Here, first term of the above equations is for C-HH transition and second term for C-LH transition.

M_b is the bulk average crystal momentum matrix that can be given by [31]

$$M_b = \left(\frac{m_0}{m_e} - 1\right)\frac{m_0 E_g (E_g + \Delta)}{6(E_g + \frac{2}{3}\Delta)} \quad (45)$$

where E_g and Δ are the energy bandgap and split-off valence band separation, respectively.

2.4 PSPICE Circuit Model

To investigate the performance of the device the physical structure of the proposed VCSEL is converted into equivalent circuit using the laser rate equations. The rate equation can be solved complicated mathematical method but it is easier to solve the problem by converting the physical into equivalent circuit and using PSPICE analysis. For this reason, PSPICE circuit model analysis technique has been chosen in the present research work. The work of Giammarco Rossi et al [37] is followed in this purpose model. Here, the active region of the VCSEL is considered. The carrier dynamic into the active region of the VCSEL is shown in fig.2.4.1. Here, SCH mean separately confined hetero-structure.

In fig.2.4.1, quasi-two-dimensional states (q-2D) collect carriers in the well with energy higher than confined states (well 2D); hence their behavior is halfway between confined 2D and bulk 3D carriers. They act as gateway state between QW confined states and the bulk region of SCH.

According to the carrier dynamics shown in fig.2.4.1, the rate equation for carrier density in the SCH

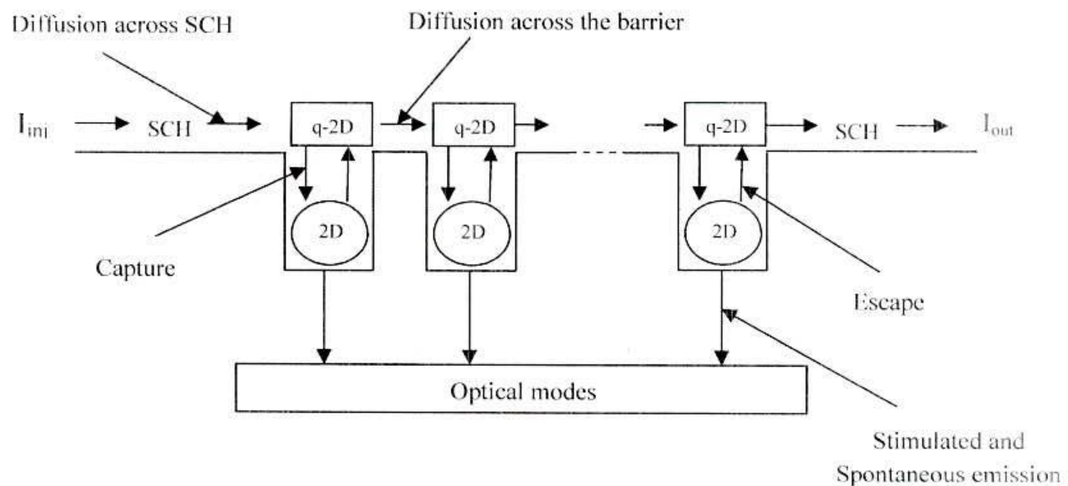

Fig.2.4.1 Carrier dynamics into the active region of the proposed VCSEL

region can be expressed by the following [37]:

$$\frac{dn_{S1}}{dt} = \frac{I_{inj}}{qV_S} - R_{S1} - \frac{I_D}{qV_S} \tag{46}$$

where n_{S1} is the carrier density in the SCH region, V_S is the volume of the SCH region, I_{inj} is the injection current in the SCH region and R_{S1} is the carrier recombination in the SCH region. The expression of the diffusion current I_D is following [37]:

$$I_D = \frac{V_S n_{S1} - V_W n_{B1}}{\tau_D} \tag{47}$$

where n_{B1} is the carrier density in the QW (quasi-two-dimensional states), τ_D is the effective space transport time that can be given by $\tau_D = L_s^2 / 2D_a$ [$D_a = D_n D_p /(D_n + D_p)$; ambipolar diffusivity]. L_s is the length of SCH region, V_W is the volume of the quantum well. The rate equation of the q-2D state in the QW is given below [37]:

$$\frac{dn_{B(j)}}{dt} = \frac{I_{D(j)} - I_{D(j+1)}}{qV_W} - R_B - \left[\frac{n_{B(j)}}{\tau_c} - \frac{n_{W(j)}}{\tau_e}\right] \tag{48}$$

being τ_c and τ_e are the carrier capture and escape time. $I_{D(j)}$ for $j \neq 1$ represents the diffusion current across the barrier between two adjacent wells and has the expression [37]

$$I_{D(j)} = \frac{V_W n_{B(j)} - V_W n_{B(j-1)}}{\tau_B} \tag{49}$$

where $\tau_B = L_B^2 / 2D_a$ is diffusion time across the barrier (L_B is the length of the barrier). The rate equation of the carrier density in confined states in the QW is given by [37]

Khulna University of Engineering & Technology
KUET
Bangladesh
Central Library

$$\frac{dn_{W(j)}}{dt} = \left[\frac{n_{B(j)}}{\tau_c} - \frac{n_{W(j)}}{\tau_e}\right] - R_{W(j)} - v_g G[n_{W(j)} s] s \quad (50)$$

where n_W is the carrier density in the confined state, v_g is the group velocity, s is the photon density, and G is the material gain which depends on the carrier density and the photon density. The expression of the material gain is [37]

$$G[n_{W(j)}, s] = \frac{G[n_{W(j)}]}{1 + g_c s} \quad (51)$$

where g_c is the gain compression factor and $G[n_{W(j)}] = G_0\left[1 + In\frac{n_{w(j)}}{N_0}\right]$. The value of G_0 and N_0 are evaluated from the carrier density-dependent calculated gain using MATLAB curve fitting tools.

The carrier density (n_{S2}) in current leaving SCH region is the summation of carrier density in SCH region and q-2D carrier density in the last QW. The rate equation of carrier density in the SCH region is given below:

$$\frac{dn_{S2}}{dt} = \frac{I_{D(last,QW)} - I_{Dout}}{qV_S} - R_{S2} - \left[\frac{n_{S2}}{\tau_c} - \frac{V_W n_{W(last,QW)}}{V_S \tau_e}\right] \quad (52)$$

where $I_{Dout} = \frac{V_s n_{s2}}{\tau_D}$ is the outgoing current from the active region. The rate equation of photon density can be expressed as following:

$$\frac{ds}{dt} = \Gamma\left[\sum_{j=1}^{k} v_g G[n_{W(j)}, s] s + \sum_{j=1}^{k} \beta R_{SP}[n_{W(j)}]\right] - \frac{s}{\tau_p} \quad (53)$$

where Γ is photon confinement factor, k is the total number of quantum well, β is the spontaneous emission factor, $R_{SP}[n_{W(j)}] = Bn_{W(j)}{}^2$ is the spontaneous emission rate; B is the radiative recombination coefficient, τ_p is the photon lifetime and can be calculated as following [38]:

$$\tau^{-1}{}_p = \left[\alpha + In(R^{-1}{}_m)/L_C\right]/v_g \quad (54)$$

where α, R_m and L_C are the material light absorption coefficient, mean mirror reflectivity and cavity length. In the above equations the recombination of carriers denoted by $R_{S,B,W}$ for different region and can be expressed as following [37]:

$$R_{S,B,W} = A_{S,B,W} n_{S,B,W} + B_{S,B,W} n^2{}_{S,B,W} + C_{S,B,W} n^3{}_{S,B,W} \tag{55}$$

where A, B and C denote the trap aided, radiative and Auger recombination coefficients. Subscripts S,B,W denote the SCH, (q-2D) carriers state (in the QW), confined QW region. In reference [34], the unit of q-2D and confined 2D carrier are volume density. For this reason, we also consider it volume density.

For converting rate equation into circuit model, equation (46) is multiplied by qV_S and then it becomes

$$V_s \frac{d(qn_{s1})}{dt} = I_{inj} - I_{s1}{}^{rec} - I_D \tag{56}$$

where $I_{s1}{}^{rec} = qV_s R_{s1}$ is the recombination current in the first SCH region. The equation (56) can be written as following:

$$C_{s1} \frac{dv_{s1}}{dt} = I_{inj} - I_{s1}{}^{rec} - I_D \tag{57}$$

where $v_{s1} = qn_{s1}$ and $C_{s1} = V_s$. The equation (57) is a capacitor node which can be described by the circuit shown in fig. 2.4.2.

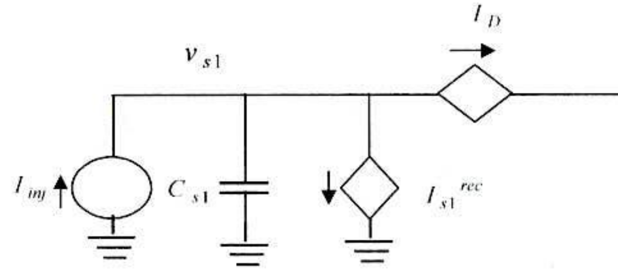

Fig. 2.4.2 PSPICE circuit model of equation (57).

In the circuit shown in fig.2.4.2, the voltage v_{s1} is related to the carrier density in the SCH region. In a similar way the rate equations (48) and (50) can be translated into equivalent circuit. The converted forms of the equations (48) and (50) are

$$C_B \frac{dv_{B(j)}}{dt} = [I_{D(j)} - I_{D(j+1)}] - I_{B(j)}^{rec} - [I_{C(j)} - I_{E(j)}] \tag{58}$$

and

$$C_W \frac{dv_{W(j)}}{dt} = [I_{C(j)} - I_{E(j)}] - I_{W(j)}^{rec} - I_{stm(j)} \tag{59}$$

where $I^{rec} = qVR$ is the recombination current, $v = qn$ and $C = V$; I_D is the diffusion current across the barrier. The capture and escape current are given by

$$I_C = \frac{qV_W n_B}{\tau_C}, I_E = \frac{qV_W n_w}{\tau_e} \tag{60}$$

As the carrier density of the current leaving SCH includes the q-2D carrier density of the last QW. So, the converted of the rate equation (52) can be written as following:

$$C_{S2} \frac{dv_{S2}}{dt} = I_{D(last,QW)} - I_{Dout} - I_{S2}^{rec} - \left[I_{C,S2} - I_{E,last(Qw)}\right] \tag{61}$$

The rate equation (53) is multiplied by $qV_W / h\nu$ and then the rate equation of the photon density becomes

$$C_{fm}\frac{dv_{fm}}{dt}=\Gamma\sum_{j=1}^{k}S_{E(j)}-\frac{v_{fm}}{R_{fm}} \quad (62)$$

where $S_E = qV_W v_g G[n_{W(j)},s]s + qV_W \beta R_{sp}[n_{W(j)}]$ is the summation of stimulated and spontaneous emission. The expression of the photon lifetime equivalent resistance on account of internal and mirror losses and optical field mode equivalent capacitance is given below:

$$C_{fm}=\frac{qV_W}{h\nu} \quad (63)$$

$$R_{fm}=\tau_P\frac{h\nu}{qV_W} \quad (64)$$

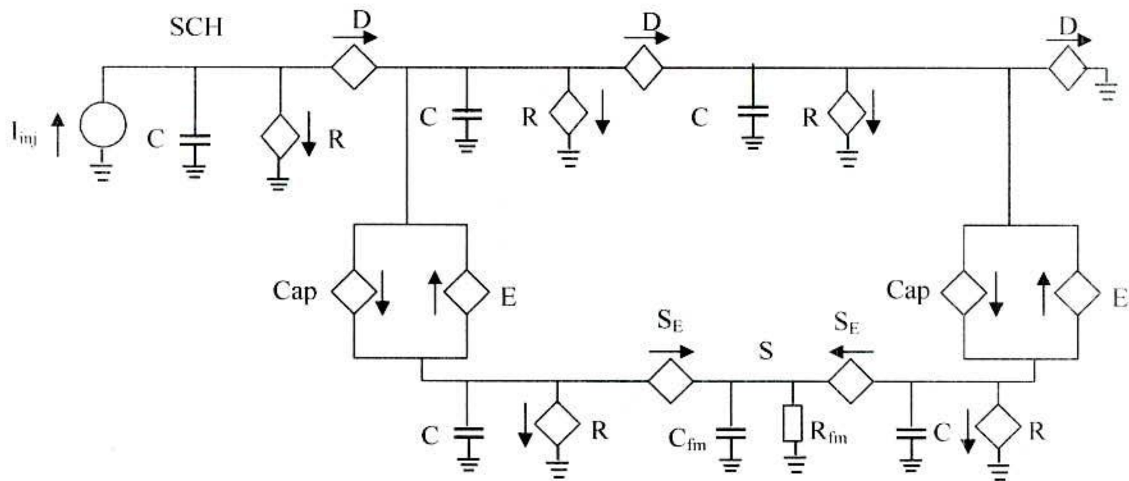

Fig. 2.4.3 Equivalent circuit of two quantum well active region, I_{inj} is the input injected current; S is the photon density; C is the capacitor as (57), R for recombination (55). Cap for capture and E for escape (60), D for drift-diffusion (48, 50), S_E for stimulated and spontaneous emission, R_{fm} for photon lifetime equivalent resistance and C_{fm} capacitance for the optical cavity (63) and (64).

The output power is determined by the following equation [38]

$$P_0 = v_{fm}\frac{\alpha_m}{\alpha+\alpha_m} \quad (65)$$

where $\alpha_m = ln(R^{-1}_m)/L_C$. The converted circuit diagram of two quantum well active region is shown in fig.2.4.3.

2.5 DBR Design

The DBR is form by alternating layers of high and low refractive index materials. The thickness of layer is equal to λ/4. The light reflected at each interface interacts constructively at the surface. The effective field reflectivity of the DBRs can be given by [39]

$$r_{eff} = \tanh\left(\sum_{i=1}^{N} \tanh^{-1}(r_i)\right) \tag{66}$$

where N is the total number interfaces of higher and lower refractive index layers and r_i is the field reflectivity for the quarter wavelength layers caused by dielectric discontinuity at each interface and is given by

$$r_i = \tanh(\frac{k\lambda}{4}) \tag{67}$$

with $\lambda = \frac{\lambda_0}{(n_1 + n_2)}$ and $k = 2\Delta n / \lambda_0$. Here, n_1 and n_2 are the low and higher refractive indices of alternating layers, $\Delta n = n_1 - n_2$ is the refractive index difference between two layers, λ_0 is the free space wavelength.

In our proposed VCSEL, $AlAs_{0.09}Sb_{0.91}$ and GaSb alternating layers are used. The refractive indices of $AlAs_{0.09}Sb_{0.91}$ and GaSb are 3.8 and 3.27 respectively. In calculating reflectivity the total number of interface is equal to twice the number of DBR pair. In selecting material, the band gap of material is also considered. The band gap of $AlAs_{0.09}Sb_{0.91}$ and GaSb are 1.66eV and 1.61eV respectively. The energy of light emitted by the laser is around 0.54eV. So, the light will not absorbed by the DBR material, as the band gap of these materials are higher. The reflectivity of the DBR as a function of number of pair is shown in fig.2.5.1. From the fig.2.5.1 it is found that for 99.13% reflectivity, 30

pairs of alternating layer are needed which are used in top mirror. In bottom mirror, 38 pairs are used which provides 99.8% reflectivity. The mean reflectivity of the two mirrors is 99.5%.

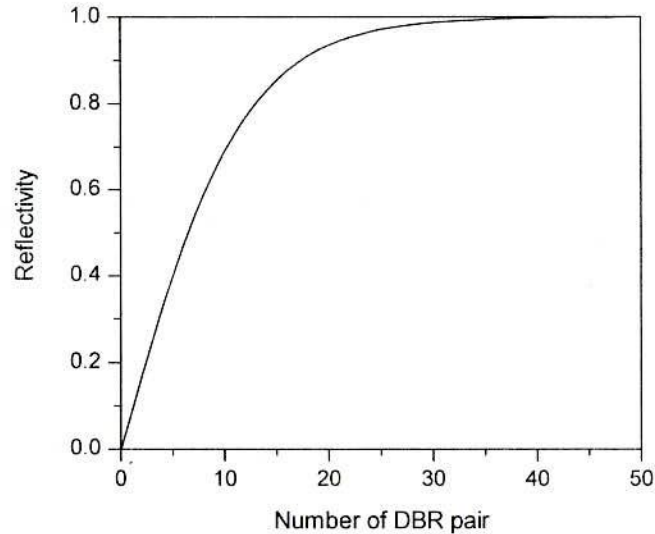

Fig. 2.5.1 Calculated mirror reflectivity for different number of $AlAs_{0.09}Sb_{0.91}/GaSb$ DBR pairs.

2.6 Model Verification

To confirm the validity of the proposed model the results obtained from the model is required to verify with the published results. To best of author knowledge, there are no experimental as well as numerical results for the proposed VCSEL structure and material system, although there existed some experimental and theoretical results on similar QW VCSEL structure in other material systems [32, 36, 40]. For the verification of the proposed model, the gain profile of InAlGaAs QW VCSEL is selected. Here, the well width is 7nm and barrier width is 5nm. The well 1.4% compressively strained. The conduction and valence band offset are given 0.25eV and 0.10eV respectively. The photon relaxation time, $\tau = 0.3\,\text{ps}$. Using the proposed model, the optical gain profile of the $In_{0.65}Al_{0.20}Ga_{0.15}As/In_{0.36}Al_{0.24}Ga_{0.15}AS$ QW VCSEL is estimated and then it is compared with experimentally reported [40] photoluminescence intensity profile. The results are summarized in fig.2.6.1. To make a comparison, the PL intensity profile and the gain profile are plotted in normalized scale as a function of wavelength. It is observed that the peak gain and peak PL intensity show good agreement. However, the PL lineshape broadening is found to be more than the lineshape obtained from simulation. The agreement indicates that our proposed model is able to calculate the energy band profiles accurately.

It is well known that the broadening of PL lineshape mainly depends on photon life time which is strongly related with material quality. The asymmetrical shape of PL intensity profile indicates that the material quality was not good. Furthermore, it is not possible to include all experimental conditions in the simulation. The parameters used in the simulation are listed in table 2.6.1. It is to be mentioned here that some of the parameters used in the simulation are not mentioned in ref. [40]. These are adjusted in order to have good agreement.

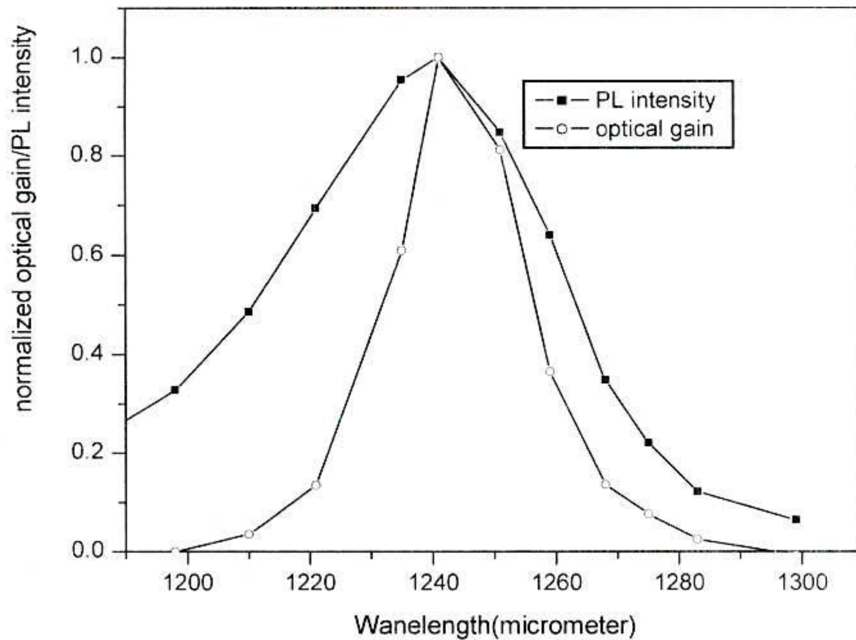

Fig.2.6.1 Comparison of normalized optical gain and PL intensity for $In_{0.65}Al_{0.20}Ga_{0.15}As$/ $In_{0.36}Al_{0.24}Ga_{0.15}AS$ QW VCSEL. The PL intensity results are from ref. [37].

Table 2.6.1: The values of material parameters used for calculation of optical gain in $In_{0.65}Al_{0.20}Ga_{0.15}As/In_{0.36}Al_{0.24}Ga_{0.15}AS$ QW VCSEL. The parameters are calculated from the parameters of binary materials GaAs, InAs, and AlAs by interpolation. The parameters of binary materials are taken from the ref. [41].

Parameter	Symbol(unit)	Well : $In_{0.65}Al_{0.20}Ga_{0.15}As$	Barrier: $In_{0.36}Al_{0.24}Ga_{0.15}AS$
Bandgap	E_g(eV)	0.8960	1.245
Luttinger parameter	γ_1 γ_2 γ_3	14.97 5.816 6.582	10.892 3.91 4.67
Conduction band deformation potential	a_c (eV)	-5.505	-6.05

Valence band deformation potential	a_v (eV)	1.318	1.4168
Shear deformation potential	b (eV) d (eV)	-1.72 -3.702	-1.688 -3.932
Elastic stiffness constant	C_{11}(10^{11} dyne/cm^2) C_{12}(10^{11} dyne/cm^2)	9.6957 4.8163	10.75 5.061

The model is further confirmed with the simulation results reported by Y.K. KUO et al [36] for GaInAsP/ InGaP QW VCSEL. The optical gain profile calculated for the $Ga_{0.88}In_{0.12}As_{0.892}P_{0.108}$/ $In_{0.49}Ga_{0.51}P$ QW VCSEL using the proposed model is compared with gain profile reported in ref. [36]. The well width was 8nm and the barrier width has not mentioned in their work. In the proposed model, both well and barrier widths are taken 8nm. According to ref [36] conduction band offset is 0.1224eV. But, the valence band offset has been not mentioned. For the verification purpose, it is calculated and found to be 0.11eV. The photon relaxation time is considered as $\tau = 0.1$ ps. Here the well is 0.473% compressively strained. Here the injection carrier density is 2.75×10^{18}cm^{-3}. The gain profile calculated by the proposed model is shown in fig.2.6.2 along with the gain profiles given in ref. [36].The parameters used for calculating the gain profiles in the pervious and in the present work are given in table 2.6.2.

Table 2.6.2: The parameters used for calculation of gain in $Ga_{0.88}In_{0.12}As_{0.892}P_{0.108}$/ $In_{0.49}Ga_{0.51}P$ QW VCSEL. The parameters are calculated from the parameters of binary materials GaAs, InP, InAs and GaP by interpolation. The parameters of binary materials are taken from the ref. [41].

Parameter	Symbol (unit)	Well: $Ga_{0.88}In_{0.12}As_{0.892}P_{0.108}$		Barrier: $In_{0.49}Ga_{0.51}P$	
		Present work	Ref. work	Present work	Ref. work
Bandgap	E_g(eV)	1.3987	1.3987	1.9139	1.9139
Luttinger parameter	γ_1	7.9704	7.9704	4.4910	4.4910
	γ_2	2.4478	2.4478	1.0584	1.0584
	γ_3	3.2663	3.2663	1.7890	1.7890
Conduction band deformation potential	a_c (eV)	-6.9158	———	-6.1110	———
Valence band deformation potential	a_v (eV)	1.1956	———	1.4893	———
Shear deformation potential	b (eV)	-1.7202	-1.7202	-1.7510	-1.7510
	d (eV)	-4.4572	———	-5.0390	———
Elastic constant	C_{11}	11.6824(10^{11} dyne/cm^2)	1186.34(GPa)	12.1194(10^{11} dyne/cm^2)	1234.21(GPa)
	C_{12}	5.3666(10^{11} dyne/cm^2)	534.23(GPa)	5.9124(10^{11} dyne/cm^2)	5922.34(GPa)

From fig.2.6.2, it is found that the value of peak gains and emission wavelength are found to be approximately same wavelength in both cases. This demonstrates that there is a good agreement between the results obtained from the proposed model with the results reported in pervious study [36]. But, the discrepancy between the two gain profiles is found for other wavelengths. It may be due to the assumptions of some parameters which are not given in the table.

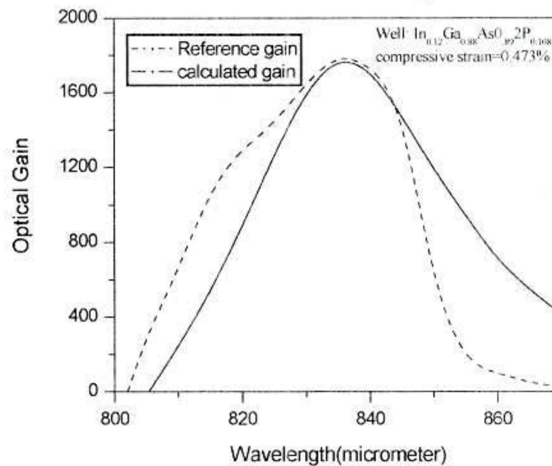

Fig2.6.2: Comparison of optical gain calculated by the proposed model with the result reported in ref.[33]

In the above discussions, the results obtained from the model are confirmed with the results reported in (001) crystal orientation. It is important to compare the results in other orientations. In this connection, the gain profile calculated by the proposed model in (110) crystal orientation is further compared with the gain profile calculated in the same orientation in ref [32]. Here, the QW material is $In_{0.7}Ga_{0.3}As$ and barrier is InGaAsP which is lattice matched to InP. The photon relaxation time is not mentioned in ref [32]. It is assumed to be 0.4ps in this case. In ref [32] the compressive strained is 1.2%. From electron affinity model, the conduction band offset is 0.1842eV and valence band is 0.09eV. In pervious work, the well width was 3.5nm and the

barrier width was not mentioned. The barrier width is assumed to be 8nm. The injection current density is $3\times10^{18}cm^{-3}$ in both reference work and proposed model. The comparison of optical gain calculated by the proposed model with the gain given in ref. [32] is shown in fig.2.6.3. The parameters used in calculating the gain profiles are listed in table 2.6.3:

Table 2.6.3:The parameters used for the calculation of gain in (110) crystal orientated $In_{0.7}Ga_{0.3}As$ QW VCSEL. The parameters are calculated from the parameters of binary materials GaAs, InP, InAs, and GaP by interpolation. The parameters of binary materials are taken from the ref. [41].

Parameter	Symbol(unit)	Well: $In_{0.7}Ga_{0.3}As$		Barrier: $Ga_{0.\ 0.2768}In_{0.\ 0.7232}As_{0.6}P_{0.4}$	
		Present work	Ref. work	Present work	Ref. work
Bandgap	E_g(eV)	0.6950	0.6950	1.01	1.01
Luttinger parameter	γ_1 γ_2 γ_3	16.0940 6.5680 7.3190	16.0940 6.5680 7.3190	11.7559 4.547 5.2247	11.7559 4.547 5.2247
Conduction band deformation potential	a_c (eV)	-5.7070	——	-5.6435	——
Valence band deformation potential	a_v (eV)	1.0480	2.560	1.1822	2.7043
Shear deformation potential	b (eV) d (eV)	-1.7700 -3.8850	-1.7700 -3.8850	-1.7545 -4.4360	-1.7545 -4.4360

Elastic constant	$C_{11}(10^{11}$ dyne/cm$^2)$ $C_{12}(10^{11}$ dyne/cm$^2)$	9.394 4.7810	9.394 4.7810	10.0671 5.1664	10.0671 5.1664
Electron affinity	χ(eV)	4.6510	____	4.4668	____

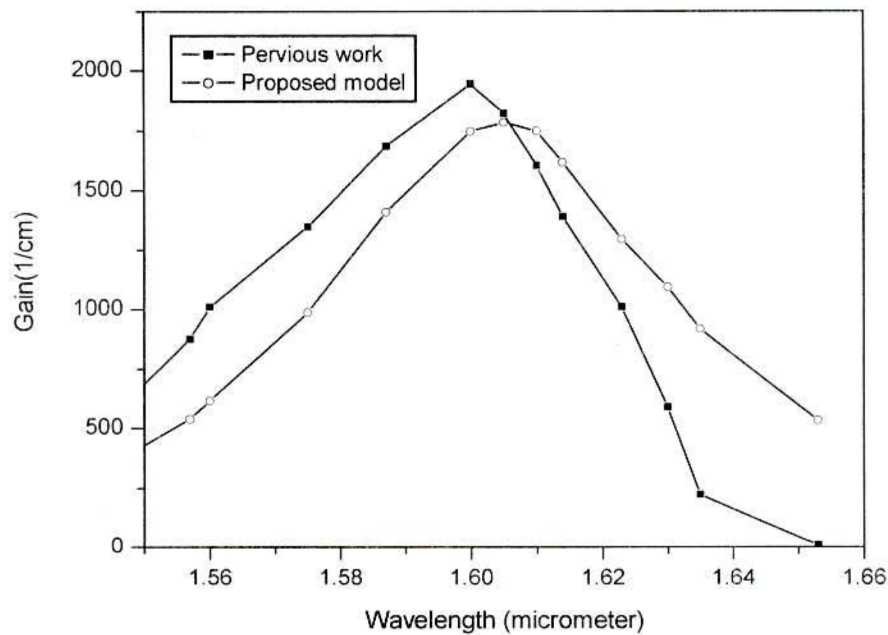

Fig.2.6.3. Comparison of optical gain calculated by the proposed model in (110) orientation with the results reported in the ref. [29]

From fig.2.6.3, it is found that the gain profile obtained in the present work shows very small shift with respect to gain profile reported in ref. [32]. The peak gain emission wavelength is 1.6μm in the pervious study and 1.605μm from the proposed model. The value of optical gain calculated by the proposed model is also found to be different from the reported gain. It may be due to assumptions of some parameters which are not mentioned in ref. [32] and these are not mentioned in table 2.6.3.

CHAPTER 3

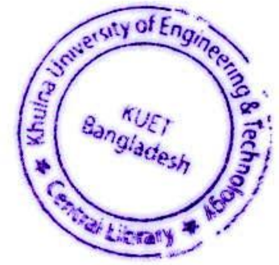

Simulation Results and Discussion

Following the theoretical analysis presented in chapter-2 the performances of the proposed GaInSb mid-infrared QW VCSEL are evaluated as a function of strains, change in crystal orientation and piezoelectric field using the parameters listed in table-3.1. In the present work, compressive strain is chosen because compressive strain in the well enhances the TE model optical gain [33]. The compositions of barrier materials are selected $Ga_{0.25}In_{0.2}Al_{0.55}Sb$, $Ga_{0.30}In_{0.15}Al_{0.55}Sb$, $Ga_{0.35}In_{0.1}Al_{0.55}Sb$, and $Ga_{0.4}In_{0.05}Al_{0.55}Sb$ so that the $Ga_{0.65}In_{0.35}Sb$ QW is compressively strained by 0.60%, 0.90%, 1.21% and 1.52% respectively. The cladding layer is lattice-matched to the barrier layer. The compositions of cladding layers are $Ga_{0.752}In_{0.248}As_{0.8}Sb_{0.2}$, $Ga_{0.74}In_{0.26}As_{0.8}Sb_{0.2}$ $Ga_{0.73}In_{0.27}As_{0.8}Sb_{0.2}$ and $Ga_{0.715}In_{0.285}As_{0.8}Sb_{0.2}$ respectively. As the physical structure of the device degrades with higher values of strain, the simulation is carried out for the maximum value of strain 1.52% in the well. The optical and electrical properties of 0.9% compressive strained QW are investigated in (001), (110), (111), (113) and (131) crystal orientations. The effect of piezoelectric field on the optical gain of the proposed VCSEL is also investigated. Furthermore, the output characteristics of the proposed laser are determined using PSPICE simulation.

It is to be mentioned here that the values of the parameters listed in table 3.1 are not available for the proposed barrier and QW materials. Therefore, the well and barrier material parameters are calculated by interpolation among the values of the binary materials listed in table 3.1.

Table 3.1: Material parameters of GaSb, InSb and AlSb [41]. The material parameters of well and barrier are calculated from these binary parameters by interpolation.

Parameter	Symbol(unit)	GaSb	InSb	AlSb
Lattice constant	a(A)	6.09602	6.47943	6.1358
Bandgap	E_g(eV)	0.813	0.24	1.612
Luttinger parameter	γ_1	13.4	34.8	5.18
	γ_2	4.7	15.5	1.19
	γ_3	6.0	16.5	0.22
Conduction band deformation potential	a_c (eV)	-7.5	-6.94	-4.5
Valence band deformation potential	a_v (eV)	0.8	0.36	1.4
Shear deformation potential	b (eV)	-2.0	-2.0	-1.35
	d (eV)	-4.7	-4.7	-4.3
Elastic stiffness constant	$C_{11}(10^{11}$ dyne/cm$^2)$	8.83	6.67	8.76
	$C_{12}(10^{11}$ dyne/cm$^2)$	4.02	3.65	4.34
Electron affinity	χ(eV)	4.06	4.4668	3.57

The bandgap of $In_{1-x}Ga_xSb$ can be calculated using the following formula [42]

$$Eg_In_{1-x}Ga_xSb = xEg_GaSb + (1-x)Eg_InSb - x(1-x)*C_InGaSb \tag{68}$$

where bowing parameter C_InGaSb = 0.415.The other parameters such as lattice constant, deformations potentials , etc. except band gap are calculated by using Veggard's law

$$P(In_{1-x}Ga_xSb) = xP(GaSb) + (1-x)P(InSb) \quad (69)$$

Where x is the composition of the material, $P(In_{1-x}Ga_xSb)$, $P(GaSb)$, and $P(InSb)$ are the parameter for InGaSb, GaSb, and InSb respectively.

To calculate the band gap of the quaternary barrier materials simple formula is used where bowing is not considered. The simple formula is also applied for calculation of other parameters of barrier materials. The formula is following [42]

$$P(Al_xGa_yIn_{1-x-y}Sb) = P(AlSb)x + P(GaSb)y + (1-x-y)P(InSb) \quad (70)$$

where x and y are the material compositions, $P(Al_xGa_yIn_{1-x-y}Sb)$ and $P(AlSb)$ are the parameters of $Al_xGa_yIn_{1-x-y}Sb$ and $AlSb$.

3.1 Band Structure and Gain in (001) Crystal Orientation

The wave function at the band edge ($k_t = 0$) of the first conduction band (C1) is calculated for different values of strain in the well and the results are presented in fig.3.1.1. It is found that the wave function penetration in the barrier is increased with increasing the values of strain. It is due to increasing potential level of electron (v_e in the well become more negative) in the well with increasing strain.

The conduction band dispersion profiles for different strains are shown in fig.3.1.2. It is found that at the band edge ($k_t = 0$) the conduction band energy shifts towards higher energy with increasing the value of strain. The conduction band edge energies found to be shifted from 0.52eV to 0.59eV for changing the compressive stain from 0.60% to 1.52%. Apart from the band edge, the energy is found to increase gradually with wave vector.

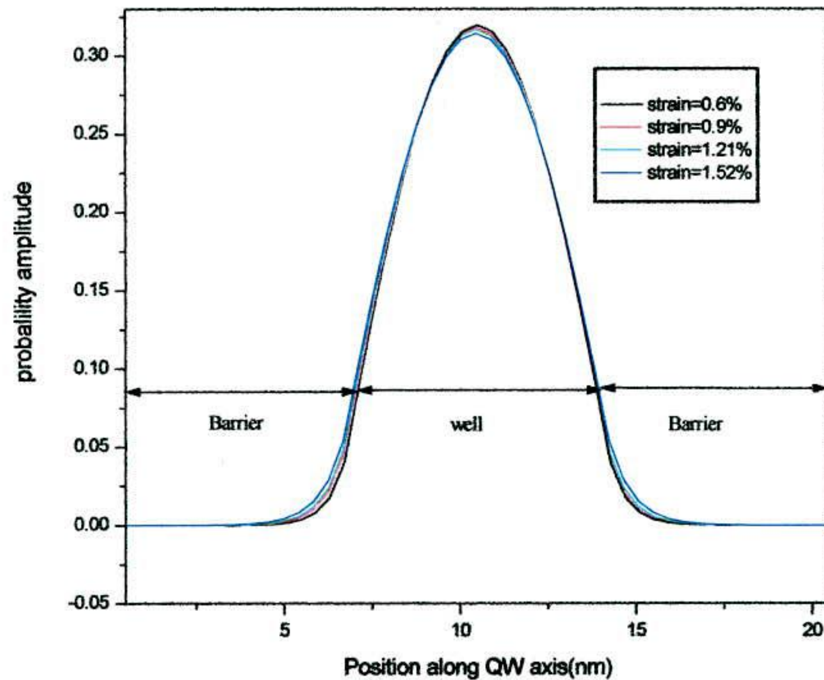

Fig.3.1.1 First conduction band (C1) wave function of $Ga_{0.65}In_{0.35}Sb$ QW estimated for different compressive strains

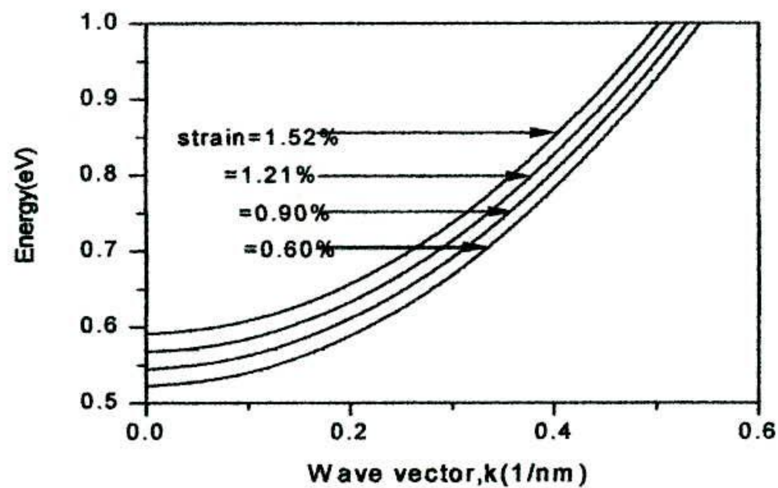

Fig.3.1.2 Compressive strain-dependent conduction band (C1) dispersion profiles for $Ga_{0.65}In_{0.35}Sb$ QW.

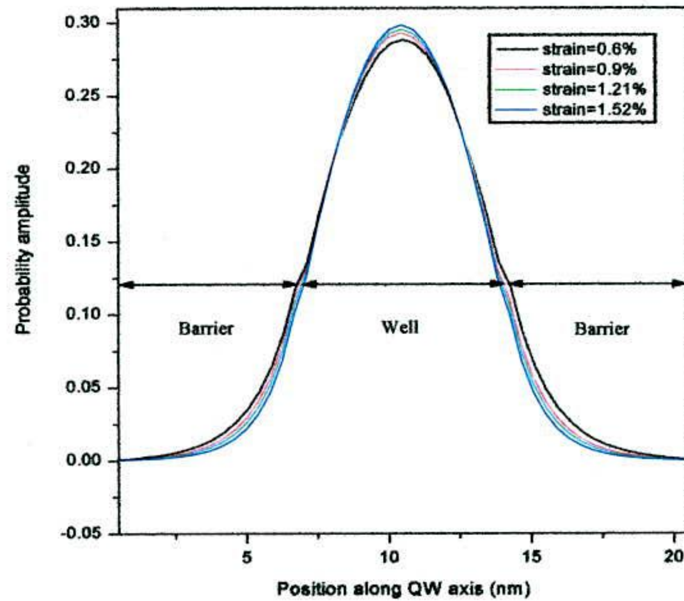

Fig.3.1.3 Compressive strain-dependent first heavy hole wave function of $Ga_{0.65}In_{0.35}Sb$ QW.

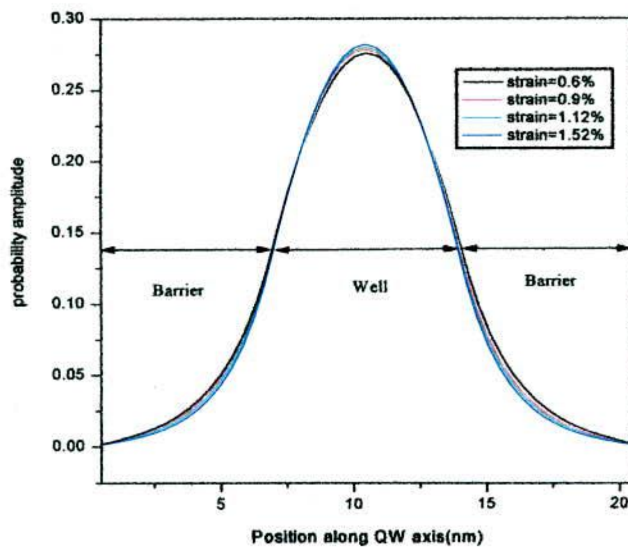

Fig.3.1.4 Compressive strain-dependent first light hole wave function of $Ga_{0.65}In_{0.35}Sb$ QW.

The wave function and energy of heavy hole (HH) and light hole (LH) are evaluated by calculating eign-vector and eign-value of $\phi_{3/2,3/2}$ and $\phi_{3/2,1/2}$ respectively. The wave functions of the first heavy hole (HH1) and light hole (LH1) at the band edge ($k_t = 0$) for different strained QWs are shown in figs.3.1.3 and 3.1.4, respectively. In both cases the wave function of holes are more confined in the well with increasing strain. Because, the valence band potential energy for hole decreases in the well with increasing strain.

The valence band dispersion profiles are also determined for the same QW. It is well established the energy separations between valence subbands are strongly depend on the state of strain. Even in unstrained condition there exists energy separation between valence subbands. The results obtained for different strain conditions are summarized in fig.3.1.5, where HH1, HH2, and HH3 indicate first, second and third heavy holes and LH1 is first light hole energy band profiles. According to the valence band dispersion profiles shown in fig.3.1.5, the top valence bands are first heavy hole sub-band due to the compressive strain in the well.

From figs.3.1.2 and 3.1.5 it is found that energy separations between C1 to HH1 and LH1 at the band edge increase due to increasing strain from 0.60% to 1.52%. The strain also

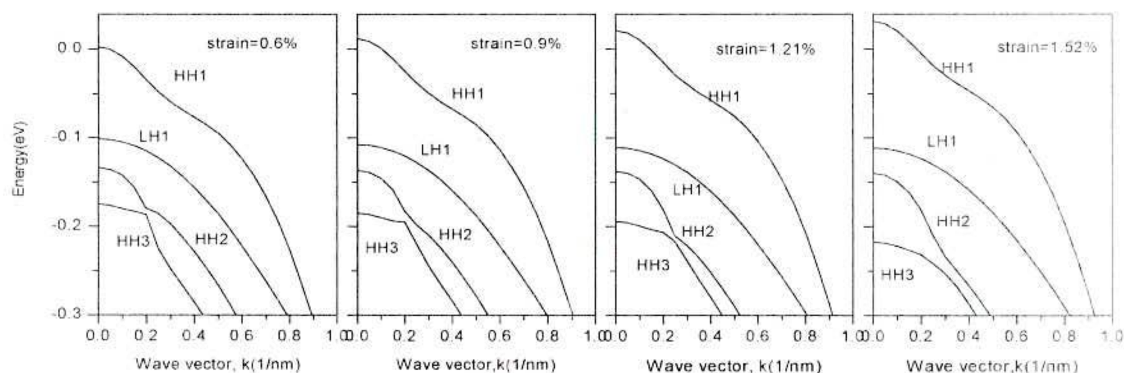

Fig.3.1.5 Compressive strain-dependent valence band dispersion profiles for $Ga_{0.65}In_{0.35}Sb$ quantum well.

separates the HH1and LH1 subbands as seen in fig.3.1.5. This indicates that the band-mixing effect between HH1 and LH1 is reduced with increasing strain.

The TE mode momentum matrix elements for the transitions C1-HH1 and C1-LH1 with different values of strain are shown in figs.3.1.6 and 3.1.7, respectively. From the figures it is found that the values of wave vector-dependent momentum matrix elements increase with increasing strain in both cases. It is due to the fact that the overlapping of wave function of electrons and holes increases with the magnitude of strains.

The optical gain spectra are calculated using equation (39) for different values of strain. The results are summarized in fig.3.1.8. For the injection carrier density $3.5\times10^{18}cm^{-3}$ the peak gains are evaluated to be $3080cm^{-1}$, $3163cm^{-1}$, $3240cm^{-1}$, and $3315cm^{-1}$,when the well is compressively strained by 0.60%, 0.90%, 1.21%, and 1.52% ,respectively. The value of peak gain is increases with increasing strain as the magnitude of momentum matrix element increases for C1-HH1 transition. The increased energy separations between HH1 and LH1 also contribute in achieving higher gain. The emission wavelength found to change from

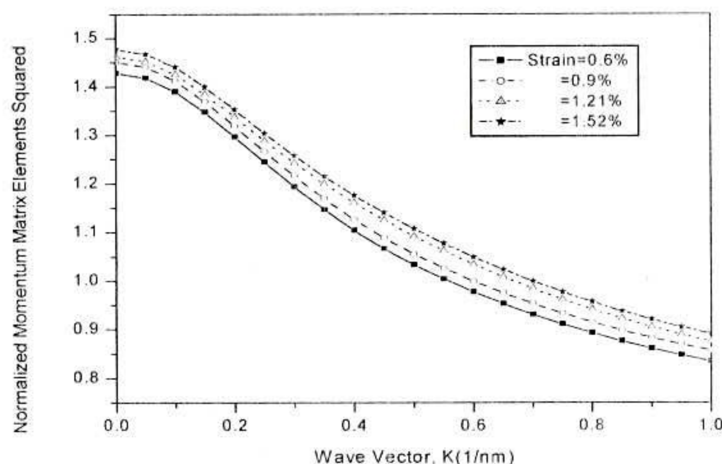

Fig.3.1.6 Strain-dependent momentum matrix element squared for C1-HH1 transition

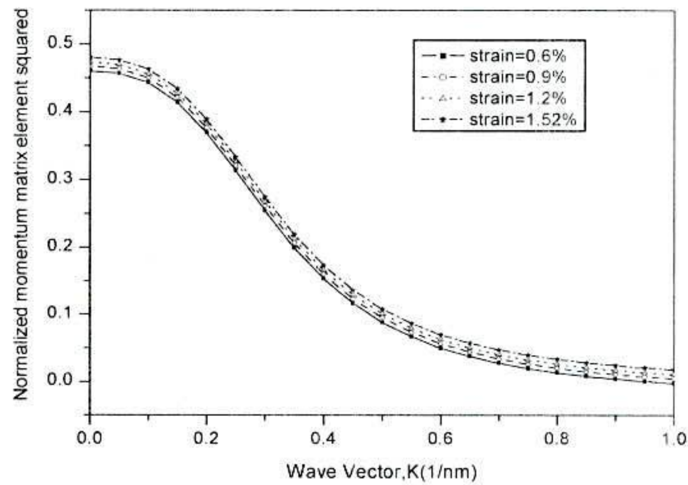

Khulna University of Engineering & Technology
KUET
Bangladesh
Central Library

Fig.3.1.7 Strain-dependent momentum matrix element squared for C1-LH1 transition

2.40μm to 2.26 μm as the energy separation increases for C1-HH1 transition with strain values.

The carrier density-dependent optical peak gains are calculated and shown in fig.3.1.9. It is found that the optical gain starts approximately at the carrier density $1.75\times10^{18}cm^{-3}$ for all

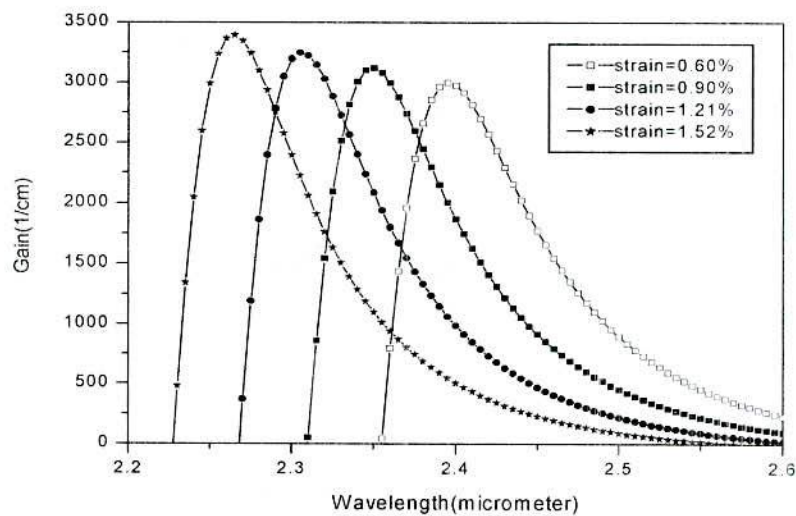

Fig.3.1.8 Calculated optical gains of $Ga_{0.65}In_{0.35}Sb$ quantum well for different value of compressive strains.

values of strain and then gradually increases with increasing carrier density as well with strain value. However, the change in optical gain is not significantly with strain when the injection current density is lower than $2.0\times10^{18}cm^{-3}$. From fig. 3.1.9, it is found that the maximum optical peak gain is evaluated when the well is 1.52% compressively strained for all values of carrier density. The optical gain also found to change significantly with carrier density when the well is compressively strained by 0.6% to 0.9%. In contrast, the change in optical gain is not remarkable when the well is strained from 0.9% to 1.52% with injection carrier density.

The differential gain plays an important role in designing high efficiency laser. It is calculated with respect to injection carrier density as a function of strain for the proposed structure and shown in fig.3.1.10. The injection carrier density is evaluated to be $2.75\times10^{18}cm^{-3}$ for all values of strain in order to have maximum differential gain.

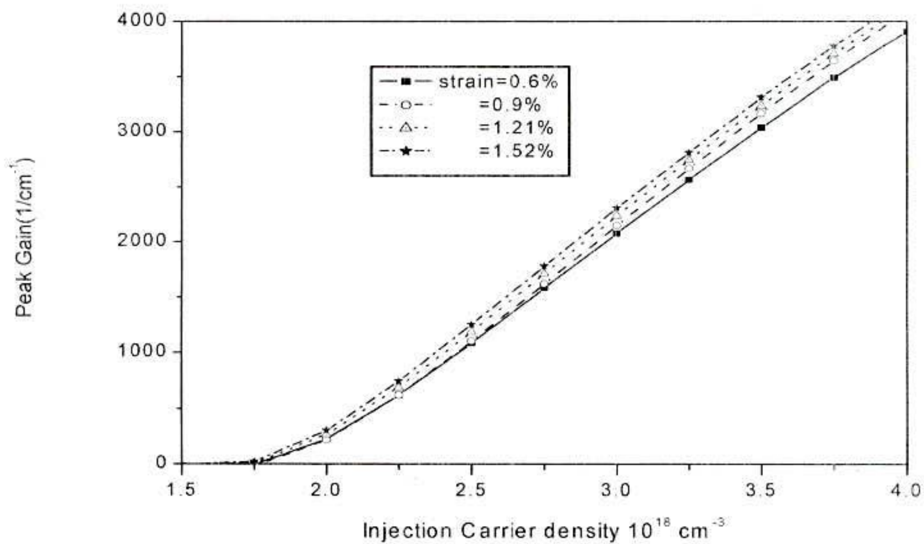

Fig.3.1.9 Peak gain as a function of carrier concentrations for different compressive strain QWs.

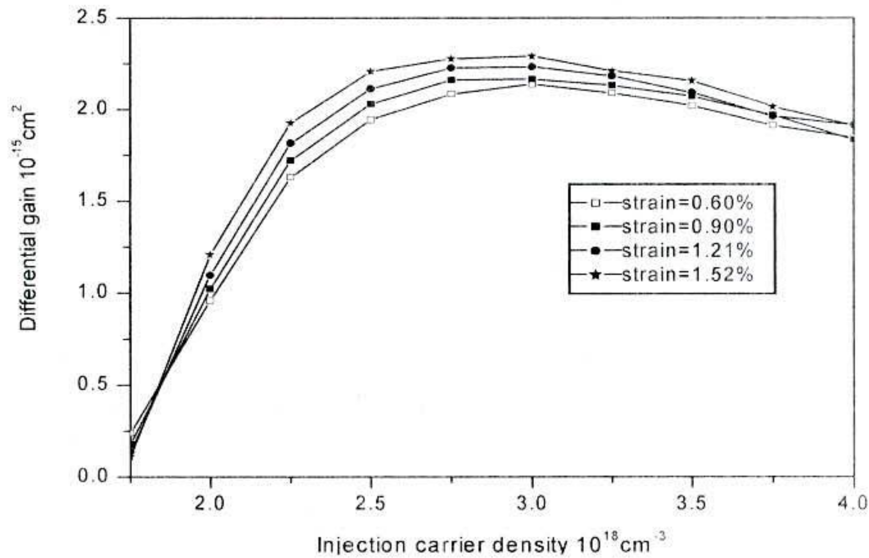

Fig.3.1.10 Differential gain with respect to injection carrier density for different compressive strained QW

3.2 Band Structures and Optical Gain in (hkl) Orientation

The optical emission properties can be changed by changing crystal orientation in the active region instead of changing the composition of the material. The orientation-dependent mathematical relationship of energy bands and optical gain are derived in section 2.2.3 in the previous chapter. Using parameters listed in table-3.1 hole wave functions are evaluated as a function of QW position. The results obtained for the first heavy hole (HH1) and light hole (LH1) wave functions at the band edge in different crystal orientations are shown in figs.3.2.1and 3.2.2. From the figures it is observed that both heavy and light hole wave functions have the same nature with crystal orientation. The wave functions of HH1 and LH1 in (113) crystal orientation are more confined in the well than other orientations. In (111) crystal orientation, higher penetration levels in the barrier are observed for the wave functions HH1 and LH1.

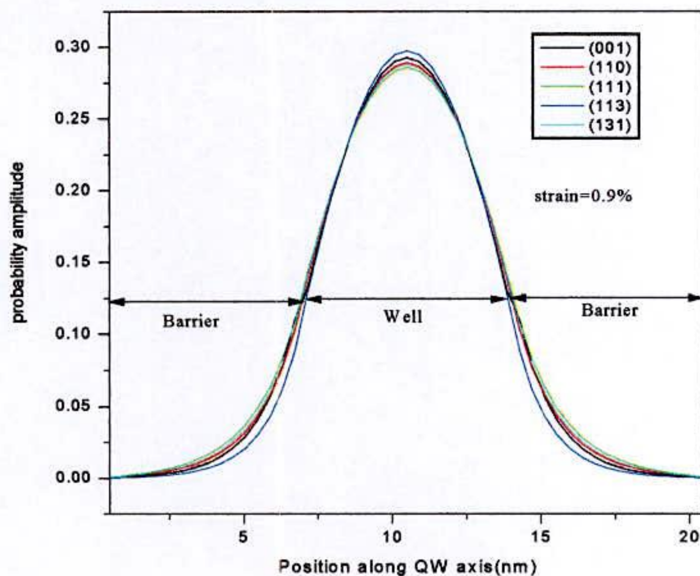

Fig.3.2.1 First heavy hole wave function of $Ga_{0.65}In_{0.35}Sb$ QW for different crystal orientations

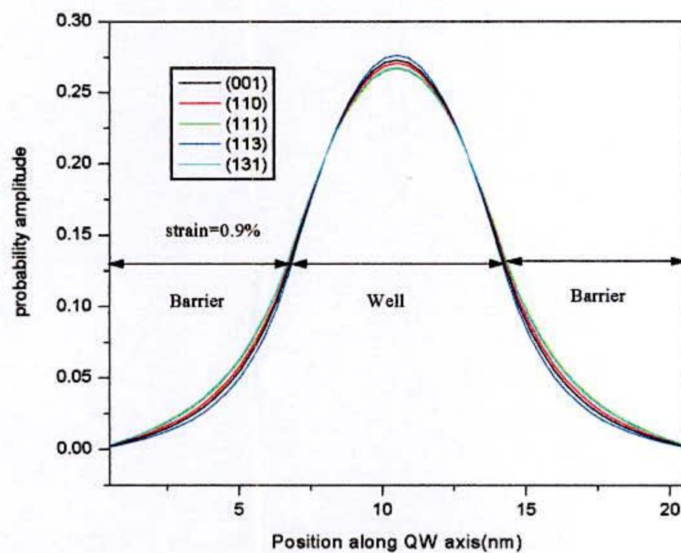

Fig.3.2.2 First light hole wave function of $Ga_{0.65}In_{0.35}Sb$ QW for different crystal orientations

The energy dispersion profiles are estimated for 0.9% strained QW in different crystal orientations. The results obtained for heavy and light holes are shown in figs.3.2.3. (a) to (e). To compare the orientation-dependent energies, the figures are plotted as a function of wave vector in the same scale. The maximum value of HH1 subband energy is found in (110) crystal orientation and minimum in (111) orientation. The orientation-dependent energy band separations at the band edge between the conduction band and valence subbands with respect to off angle (θ) are shown in fig.3.2.4. It is found that the energy separation between C1 and HH1 is maximum in (111) crystal orientation and minimum in (110) orientation. The zone-center splitting between the HH1 states and the LH1 states in 0.9% compressive strained QW is evaluated maximum in (113) orientation and the minimum in (111) orientation. The momentum matrix elements of C1-HH1 and C1-LH1 transitions for different crystal orientations are shown in figs.3.2.5 and 3.2.6. In both cases, the maximum value of momentum matrix element is evaluated in (113) orientation and minimum in (111) orientation as the overlapping function of electrons and holes is maximum and minimum in (113) and (111) orientations, respectively.

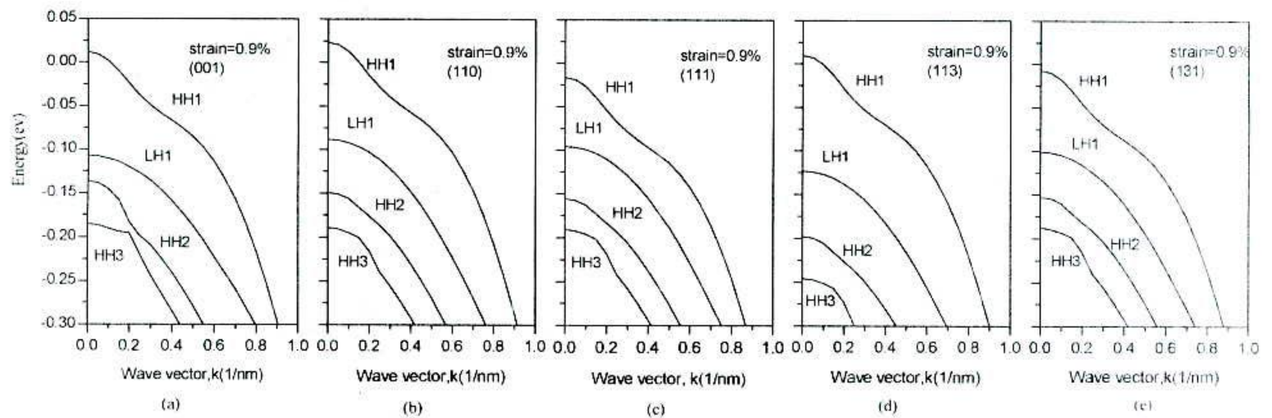

Fig.3.2.3 Valence band dispersion profiles of 0.9% compressive strained $Ga_{0.65}In_{0.35}Sb$ QW (a) (001), (b) (110), (c) (111), (d) (113), and (e) (131)

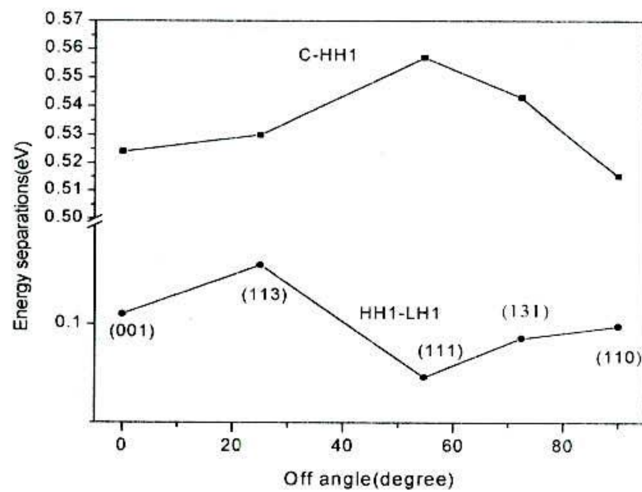

Fig.3.2.4 Orientation-dependent energy separations between the conduction and valence subbands for GaInSb strained QW

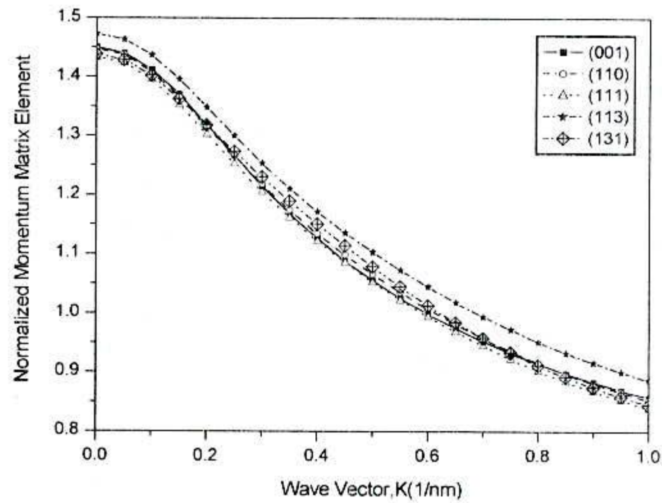

Fig.3.2.5 Crystal orientation-dependent normalized momentum matrix element square for C1-HH1 transition

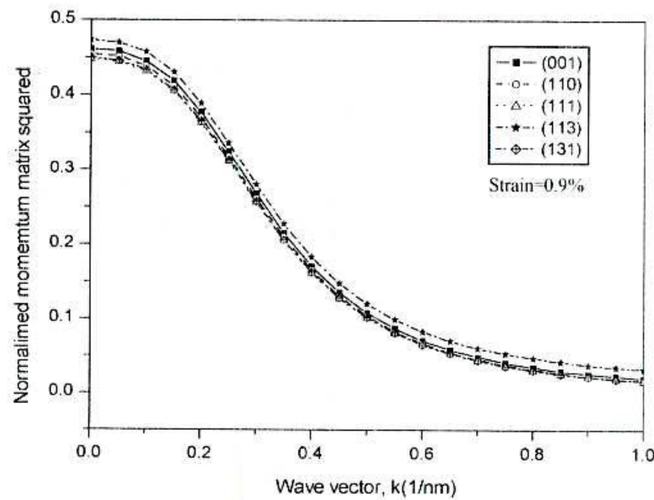

Fig.3.2.6 Crystal orientation-dependent normalized momentum matrix element square for C1-LH1 transitions

Using equation (39), we have calculated the optical gain spectra in different crystal orientations and shown in fig. 3.2.7. The results are evaluated for the injection carrier density $3.5\times10^{18}cm^{-3}$. The amount of peak gains are estimated to be 3115, 3080, 2790, 3415, and

2940cm^{-1} respectively, in (001), (110), (111), (113), and (131) crystal orientations. The maximum gain is found in (113) crystal orientation, because the value of momentum matrix element for the transition from C1 to HH1 in (113) crystal orientation is higher than other crystal orientations. The separation between HH1 and LH1 also found maximum in this orientation which is also the cause of higher gain. The peak emission wavelength changes from 2.4μm to 2.25μm for the change in crystal orientation from (110) to (111).

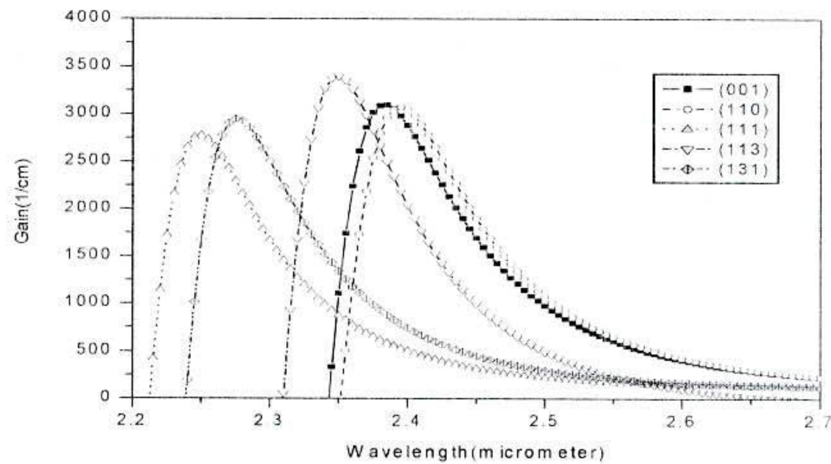

Fig.3.2.7: Optical gains evaluated in different crystal orientations for 0.9% compressive strained $Ga_{0.65}In_{0.35}Sb$ QW.

There is a strong correlation between the peak optical gain and injection carrier density in a particular crystal orientation. Using equation (39 to 42) carrier density-dependent optical gain in different crystal orientations is calculated and shown in fig.3.2.8. It is found that starting of optical gain is highly dependent on the injection carrier density in a particular crystal orientation. The carrier density required to start gain is found to be higher in (111) orientation and smaller in (113) orientation. It is also found that at lower injection carrier density ($2\text{~}3\times10^{18}cm^{-3}$), output optical power characteristics in (001) and (110) crystal orientations are very much close to each other. But, at higher injection region there is a small difference in

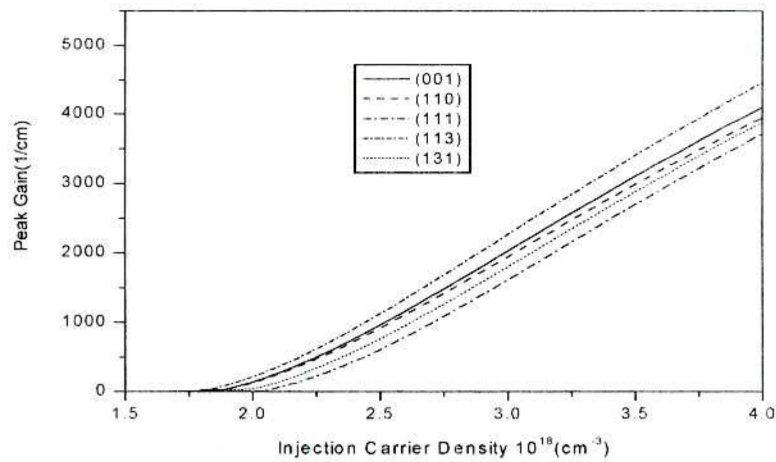

Fig.3.2.8: Carrier density-dependent optical gain in different crystal orientations for 0.9% compressive strained $Ga_{0.65}In_{0.35}Sb$ QW.

peak gain in these orientations. As seen in fig.3.2.8, the highest optical gain is obtained in (113) orientation and lowest in (111) orientation with injection carrier density.

The crystal orientation-dependent differential gain is calculated and shown in fig.3.2.9. According to fig.3.2.9, the maximum differential gain is found to be $2.18\times10^{-15}cm^2$, $2.16\times10^{-}$

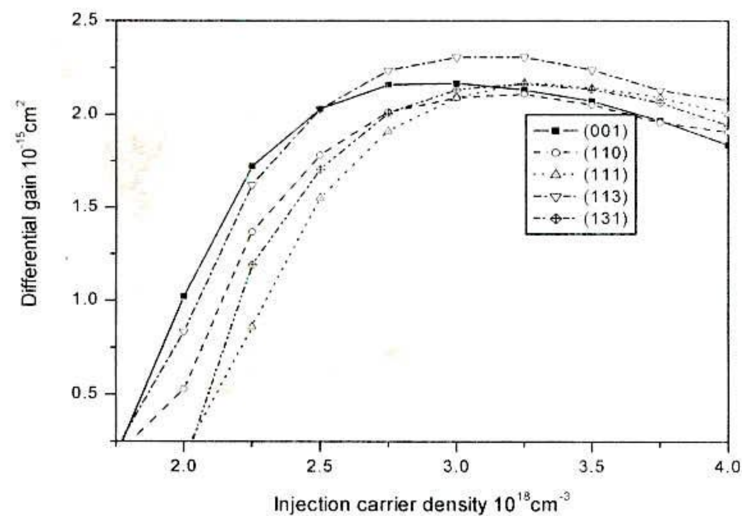

Fig.3.2.9 Differential gain with respect to injection carrier density in different orientations

^{15}cm^2, 2.13×10^{-15}cm^2, 2.32×10^{-15}cm^2, and 2.78×10^{-15}cm^2 in the (001), (110), (111), (113) and (131) crystal orientations, respectively. The maximum differential gains are obtained when the injection carrier densities 2.75×10^{18}cm^{-3} and 3.0×10^{18}cm^{-3} in (001) and (113) crystal orientations. For (110), (111), and (131) crystal orientations, the maximum differential gains are evaluated when the injection carrier density is 3.25×10^{18}cm^{-3}.

3.3 Effect of Bands shift Due to Piezoelectric Field

The performances of the optical devices are changed in presence of piezoelectric filed [12]. In ref. [12] InGaAsP/InP material system has been considered. The shift in energy due to piezoelectric field between first conduction band and first heavy hole bands are calculated in (110), (111), (113), and (131) crystal orientations. It is found that the shifts in energy levels strongly depend on the quantum well length and are found to be small for small quantum well length. The magnitude of piezoelectric field and corresponding energy shift are calculated for 15nm quantum well length in different crystal orientation and listed in table 3.3.1.

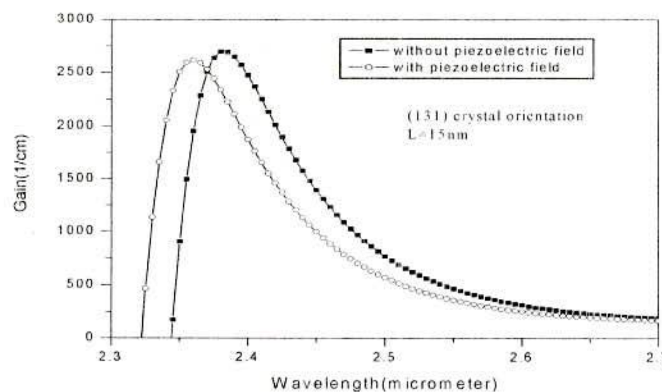

Khulna University of Engineering & Technology
KUET
Bangladesh
Central Library

Fig. 3.3.1 Effect of piezoelectric field on emission profile for 15nm 0.9% compressive strained $Ga_{0.65}In_{0.35}Sb$ quantum well in (131) crystal orientation

From table 3.3.1, it is found that the amounts of energy shift due to piezoelectric fields are small because of low piezoelectric constant of GaInSb material. Using the shift in energy bands, the optical gain profile for 15nm length 0.9% compressive strained QW is calculated in (131) crystal orientation and shown in fig.3.3.1. To compare the optical gain profile calculated in (131) crystal orientation without considering piezoelectric filed is also plotted in fig.3.3.1. It is clear that the peak emission wavelength shifts from 2.38μm to 2.36μm due to piezoelectric effect. The value of optical gain is evaluated 2630cm^{-1} in presence of piezoelectric field. The similar result is found to be 2700cm^{-1} when piezoelectric field is not considered. This indicates that the optical gain is decreased 70cm^{-1} in presence of piezoelectric filed.

Table 3.3.1: Crystal orientation-dependent energy shifts due to piezoelectric fields for 0.9% strained QW

Crystal Orientation	Piezoelectric fields(V/m)	Conduction band energy shifts, ΔE^c (meV)	Valence band energy shifts, ΔE^{hh} (meV)
(110)	8.38×10^5	0.0306	0.2527
(111)	1.57×10^6	0.1077	0.8871
(113)	6.25×10^4	0.0001	0.0014
(131)	3.93×10^6	0.6750	5.5601

To understand the shift in peak emission wavelength due to piezoelectric field with higher value of strain, similar results are calculated in (131) orientation for 1.52% compressively strained QW. The optical emission profiles obtained in presence of piezoelectric and without piezoelectric are shown in fig.3.3.2. It is found that the peak emission wavelength shifts from 2.25μm to 2.22μm and peak gain decreases $85cm^{-1}$ for 1.52% strained QW due to piezoelectric field. This demonstrate that at higher value of strain more shift in peak wavelength can be obtained due to piezoelectric field with reduction of peak gain in case of proposed laser structure.

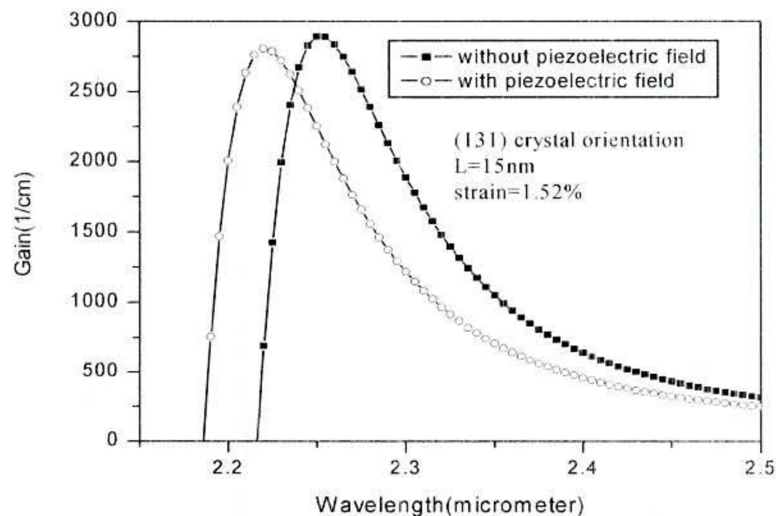

Fig.3.3.2 Effect of piezoelectric field on emission profile for 15nm 1.52% compressive strained $Ga_{0.65}In_{0.35}Sb$ quantum well in (131) crystal orientation

3.4 Output Characteristics

To understand the performance of the proposed VCSEL it is very much important to study its output characteristics. The output optical power-input current characteristics are investigated from PSPICE analysis of the equivalent circuit developed for the proposed laser structure.

The procedures of converting mathematical model into equivalent electrical circuit for the proposed VCSEL structure have been discussed in section 2.4. For the simulation, the parameters used are shown in table 3.2. In this simulation work, it is assumed that the gain profiles of all QWs are same. The optical power-injection current characteristics of 0.9% compressively strained well are shown in fig.3.4.1 for different number of wells.

3.2: Material parameterials used for evaluating output optical power characteristics. These parameters are calculated from the binary parameters of GaSb, InSb, AlSb and AsSb by interpolation. The binary parameters are taken from ref. [41].

Name	Symbol	value
Optical confinement factor(mean value)	Γ	0.020
Am bipolar diffusivity	D_a	4.4 cm^2s^{-1}
Barrier width	L_B	7nm
Well width	L_W	7nm
Gain suppression factor	g_c	5×10^{-17}
Carrier capture time	τ_C	0.97ps
Carrier escape time	τ_e	6ps
Internal loss of the cavity	α	$30cm^{-1}$
Mean mirror reflectivity	R_m	0.995
Shockley–Read–Hall coefficient of well	A_W	$2.4\times10^8s^{-1}$
Radiative recombination coefficient of well	B_W	1.5×10^{-11} cm^3s^{-1}
Auger recombination coefficient of well	C_W	7×10^{-27} cm^6s^{-1}
Shockley–Read–Hall coefficient of SCH	$A_{S,B}$	$5\times10^8s^{-1*}$
Radiative recombination coefficient of SCH	$B_{S,B}$	3.6×10^{-11} cm^3s^{-1*}
Auger recombination coefficient of SCH	$C_{S,B}$	8×10^{-30} cm^6s^{-1*}

* These parameters are calculated by interpolation with respect to bandgap.

From fig.3.4.1 it is found that the output optical power increases with number of QW. But, if the numbers of quantum wells are more than three, the output optical power does not increase significantly. As the number of QWs increase, the optical gain increases as well as optical losses and carrier transport time increases. For the combined effect of the above facts, it is thought that the optical power remains same when the number of QWs three and above. The threshold current for the proposed laser is dependent on the number of QWs as seen in fig.3.4.1. When the number of QW N=1, the threshold current is found to be 1mA. The same is found to be 0.8mA when the number of QW increases from N=2 to N=4. As the optical output power-injection current characteristics approximately same for N=3 and N=4, the threshold current for these case remain same.

The strain-dependent optical output power-input current characteristics are evaluated for the number of QWs N=3 and shown in fig.3.4.2. It is found that at lower injection current (2.0mA) the output optical power is approximately constant for all values of strains.

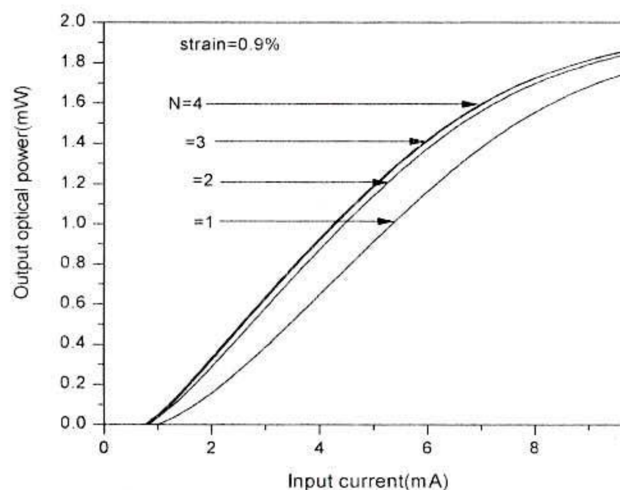

Fig.3.4.1.Output optical power-input current characteristics of $Ga_{0.65}In_{0.35}Sb$ quantum well for different numbers of QWs.

However, the output optical power increases gradually with strain when the injection currents are higher than 2.0mA. Here the maximum optical power is obtained for 1.52% strained QW due to higher optical gain in this value of strain. It is also observed in fig.3.4.2 that the output optical power tends to saturate with increasing injection current for all values of strains. It occurs due to gain compression factor. Furthermore, for a constant injection, particularly, in the higher injection current range, the optical power is found to be saturated with increasing strain.

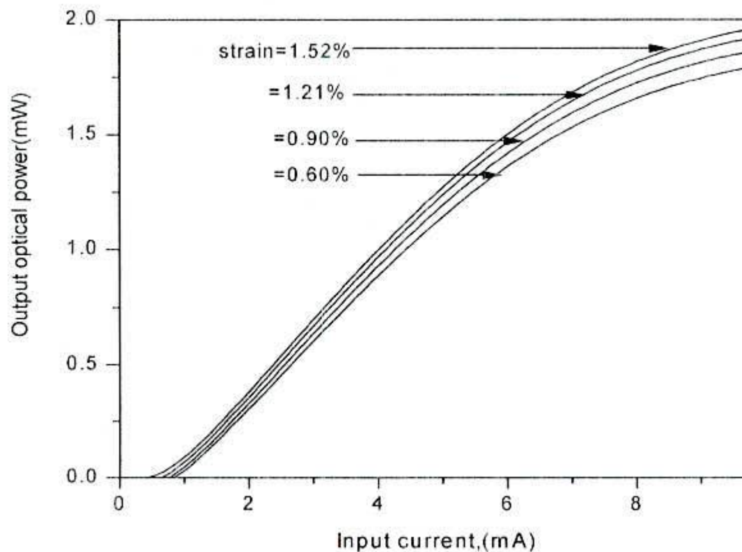

Fig.3.4.2 Optical power characteristics of $Ga_{0.65}In_{0.35}Sb$ quantum well for different value of strain when number of QW is three

The optical power-injection current characteristics determined for 0.9% compressive strained well in different crystal orientations are shown in fig.3.4.3. It is found that the maximum optical power and minimum threshold current are obtained in (113) orientated VCSEL structure. The value of the minimum threshold current is found to be 0.75mA in (113) orientation. On the other hand, the maximum threshold current is evaluated to be 1mA in

(111) crystal orientation. It is also found in fig.3.4.3, that the optical power characteristics in (110), (001) and (131) are closed to each other. Because, the gain characteristics of the above mentioned QW structures are almost same. As seen in fig.3.4.3 the differences among the optical power for different QW structures are comparatively smaller at lower input currents than of these at higher input currents.

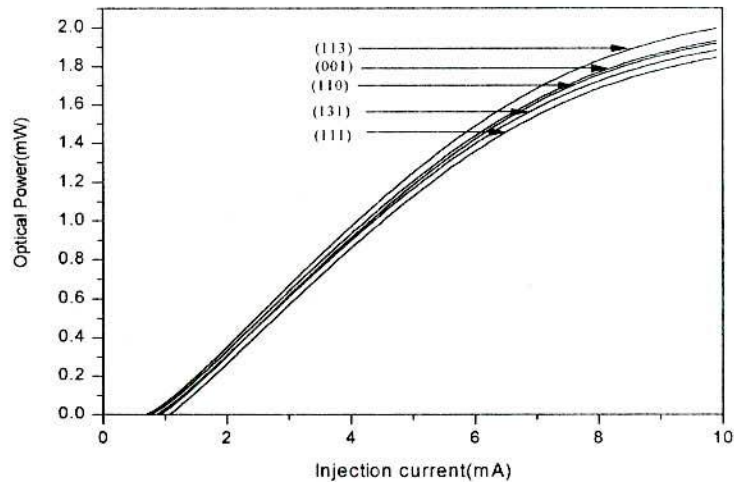

Fig.3.4.3.Output optical power-input current characteristics of 0.9% compressive strained $Ga_{0.65}In_{0.35}Sb$ QW for different crystal orientations

CHAPTER 4

Concluding Remarks

4.1 Conclusion

In the present research, the physical structure of GaInSb/GaAlInSb vertical cavity surface emitting mid-infrared QW laser is proposed in (001) as well as in arbitrary crystal orientations. Mathematical model for the proposed laser is developed using Schrödinger equation taking into account of strain, change in crystal orientations and piezoelectric field. To evaluate the optical emission and output optical power-input current characteristics for different values of strain and crystal orientations Schrödinger equations for conduction and valence band are solved using finite difference method. To confirm the validity of the proposed model, the results obtained from the model are compared with the experimental and simulation results reported in pervious studies [32, 36, 40]. To investigate the output optical power-input characteristics the physical structure of the proposed VCSEL is converted into equivalent circuit model and then PSPICE analysis is carried out. Using the model, the numerical results estimated for the proposed VCSEL demonstrate that the momentum matrix elements, wave functions, energy band dispersion profiles and output optical power characteristics are strongly depend on strain, crystal orientations and piezoelectric field.

From the wave functions evaluated in (001) crystal orientation it is observed that the wave functions for electrons are more confined in the well than the wave functions of heavy and light hole. It is also found that the wave function of electrons penetrate more in the well with increasing strain. The results are found opposite for the holes wave functions. The transition momentum matrix elements depend on the overlapping of electron and hole wave functions.

The overlapping of electrons and holes wave functions (both heavy and light hole) increases with strain. As a result, magnitudes of the transitions matrix elements increase. The positions of the emission wavelength depend on the energy separation between conduction and valence band. The energy band separations from conduction band to heavy and light hole increases with increasing strain which leads to shift emission wavelength shift in shorter wavelength. The value of optical gain increases with strain as the energy band separations and transitions matrix elements are increased with strain. The optical gain in (001) crystal orientated laser structure starts when the injection carrier density approximately 1.75×10^{18} cm^{-3} for all values of strain. From the injection carrier density-dependent optical gain characteristics it is found that higher gain is obtained for any injection carrier density when the well is 1.52% compressively strained. The differential gain is found maximum when the injection carrier density is 2.75×10^{18}cm^{-3} for all values of strain. Among different strained QWs, higher differential gain is evaluated for 1.52% strained QW.

The conduction band and valence band wave functions evaluated in (001) and arbitrary orientations as a function of QW position indicate that the heavy and light hole wave functions are confined more in the QW in (113) crystal orientation than (001), (110), (111), and (131) orientations. The transition momentum matrix elements and valence band energy separations are also found to be higher in (113) orientation. For these reasons the higher optical gain is obtained in (113) crystal orientation. The opposite results are found in (111) orientation leading to minimum optical gain in this orientation. The maximum emission wavelength (2.4μm) is evaluated in (110) orientation and minimum (2.25μm) in (111) orientation due to the maximum energy separations in (111) orientation and minimum in (110) orientation. The optical gain starts with minimum injection carrier density of 1.75×10^{18}cm^{-3} for the 0.9% compressively strained QW grown in (113), (001), and (110)

orientations. However, the required injection carrier density is found to be $2.0\times10^{18}cm^{-3}$ to start gain in (111) orientation. The carrier density-dependent higher optical gain is evaluated in (113) orientation and lower in (111) orientation. The maximum differential gain is found to be $2.18\times10^{-15}cm^2$, $2.16\times10^{-15}cm^2$, $2.13\times10^{-15}cm^2$, $2.32\times10^{-15}cm^2$, and $2.78\times10^{-15}cm^2$ in (001), (110), (111), (113) and (131) crystal orientation, respectively.

The influence of piezoelectric field on the optical gain and peak emission wavelength is found to be not so significant for the proposed laser structure. The gain decreases $70cm^{-1}$ and emission wavelength shifts from 2.38μm to 2.36μm due to piezoelectric field in (131) orientated 15nm 0.9% compressively strained QW structure. For 1.52% compressively strained QW, the emission wavelength found to be shifted from 2.25μm to 2.22μm and optical gain decreased by $85cm^{-1}$due to piezoelectric field in presence of piezoelectric field. Among different orientations, strain-induced piezoelectric field and piezoelectric field-dependent energy shift are found to be maximum in (131) orientation.

From the simulation of optical power-input current characteristics, optimum number of QWs in the active region is found be three for the proposed VCSEL. The minimum threshold current is evaluated to be 0.8mA in (001) orientated laser structure when the well is 0.9% compressively strained. The optical power is found to be higher when the QW is highly strained. Among the different crystal orientations, the higher optical power is evaluated in (113) orientation and the minimum threshold current is found to be 0.75mA in this orientation. A suitable DBR design is designed for the proposed VCSEL whose mean reflectivity of 99.5% is found for 30 and 38 pairs alternating layers of $AlAs_{0.09}Sb_{0.91}$ and GaSb are used in top and bottom mirror.

4.2 Suggestion for Future Work

Present research work is concerned with modeling and performance analysis of mid-infrared QW VCSEL. The electrical and optical properties of mid-infrared QW VCSEL have been investigated accurately by solving conduction and valence band Schrödinger equations in finite difference method. During research work, it found that potential for electron and hole is important for evaluating energy bands. In our present work, the potential level of electron and hole are calculated according to the electron affinity model at the junction. But the potential can calculated more accurately by solving self-consistent Schrödinger-poisson's equations. So, the present work can be extended by calculating the potential profiles solving the self-consistent Schrödinger-poisson's equations.

The performances of the QW VCSEL also depend upon how many bands have been considered in modeling. Presently, conduction band, heavy hole band and light hole band have been considered. Here 4×4 Hamiltonian matrix has been solved to evaluate energy bands. In future work spin split-off band can be include by solving 6×6 Hamiltonian matrix.

In present work the influence of piezo-electric field has been included by using QCSE theory. QCSE theory gives the energy band shifts only. The effect of piezo-electric field can be included more accurately by considering piezoelectric field related Hamiltonian matrix. As the piezo-electric constant of Nitride-based material system is higher, it is expected that the effect of piezo-electric filed will be effective in Nitride-based VCSEL. So, in future work the performances of Nitride-based VCSEL can be investigated with the modified model.

The active region of the proposed VCSEL is symmetric QW and it is found that its emission wavelength shifts for changing the value of strain, crystal orientation and piezo-electric field. But, if asymmetric QWs are used in the active region of the proposed VCSEL, then it is

expected that different emission wavelengths are found depends on injection current density. So, in future, the performances of asymmetric QW VCSEL can be investigated.

PSPICE circuit simulation techniques have been used to evaluate the output performances of the devices. The output performance can be evaluated by solving the rate equations with the help of numerical methods in future.

References

[1] William T. Silfvast, Laser Fundamentals, Cambridge University Press, 1998.

[2] A. L. Schawlow and C. H. Townes, "Infrared and Optical Masers," Physical Review, vol.112, no.6, pp. 1940-1949, December 1958.

[3] T.H. Maimon, " Stimulated optical radiation in ruby," Nature, vol. 187, pp.493-494, 1960.

[4] A. Javan, W, B., Bennett, Jr., and D. R. Herriott, "Population Inversion and Continuous Optical Maser Oscillation in a Gas Discharge Containing a He-Ne Mixture," Phys. Rev. Letters, vol. 6, no.3, pp. 106-110, February 1961.

[5] L. F. Johnson, G. D. Boyd, K. Nassau, and R. R. Soden , "Continuous Operation of a Solid-State Optical Maser," Physical Review, vol.126, no.4, pp. 1406-1409, May 1962.

[6] R. N. Hall, G. E. Fenner, J. D. Kingsley, T. J. Soltys, and R. O. Carlson, "Coherent Light Emission From GaAs Junctions," Physical Review Letters, vol.9, no.9, pp. 366-368, November 1962.

[7] Pallab Batcharry, Semiconductor Optoelectronic Devices, Prentice Hall: second edition, 1996 .

[8] K. Iga, "Surface emitting laser–its birth and generation of new optoelectronics field," IEEE journal of selected topics quantum electron., Vol. 6, no. 6, pp. 1201–1215, 2000.

[9] H. Soda, K. Iga, C. Kitahara, and Y. Suematsu, "GaInAsP/InP surface emitting injection lasers," Japaness journal of Applied Physics, Vol 18., pp. 2329–2330, 1979.

[10] M. R. McDaniel, D. L. Huffaker, and D. G. Deppe, "Hybrid dielectric/metal reflectorfor low threshold vertical cavity surface emitting lasers," Electron Letter, Vol. 33,no. 20, pp. 1740–1741, 1997

[11] J. Boucart, C. Starck, F. Gaborit, A. Plais, N. Bouche, E. Derouin, L. Goldstein,C. Fortin, D. Carpentier, P. Salet, F. Brillouet, and J. Jacquet, "1 mW CW-RT Monolithic VCSEL at 1.55 µm," IEEE photonic technology Letter, Vol. 11, no. 5,pp. 629–631, 1999.

[12] Yae Okuno, "Polarization control of long-wavelength vertical cavity surface emitting laser (VCSEL) fabricated by orientation-mismatched wafer bonding," PhD thesis, University of California, Santa Barbara, 2004.

[13] Sahba Talebi, Werner Hofmann, Pouria, G. Bohm, Marks Ortsiefer, Ezra Kwok, Markus-Christian, Amann and Lukas Chrostowski, " Optical absorption glucose using 2.3µm vertical cavity semiconductor laser," IEEE photonics thecnology letters, vol. 20, no.11, pp. 930-932, June 2008.

[14] Matthew R McCurdy, Yury Bakhirkin, Gerard Wysocki, Rafal Lewicki and Frank K Tittel, "Recent advances of laser-spectroscopy based techniques for applications in breath analysis," Journal of Breath Research, vol.1, no.1, pp. 014001 (12pp), September 2007.

[15] C. Gmachl, D. L. Sivco, M. L. Peabody, and A.Y. Cho, "Laser-based mid-infrared reflectance imaging of biological tissues," Optical Society of America, vol. 12, no.1, pp. 208-219, January 2004.

[16] Sandip Pal, Krikor B. Ozanyan and Hugh McCann, "A Spectroscopic Study for detection of Carbon-monoxide using Mid-Infrared Techniques for Single-pass measurement," Journal of Physics: Conference Series 85 (2007) 012020, IOP Publishing, doi:10.1088/1742-6596/85/1/012020.

[17] William W. Bewley, Christopher L. Felix, Igor Vurgaftman, Edward H. Aifer, Linda J. Olafsen, Jerry R. Meyer, Lew Goldberg, and David H. Chow, "Mid-Infrared Vertical-Cavity Surface-Emitting Lasers for Chemical Sensing," Applied Optics, vol.38, no. 9, pp. 1502-1505, March 1999.

[18] Paul Corrigan, Rainer Martini, Edward A. Whittaker, Clyde Bethea, "Quantum cascade lasers and the Kruse model in free space optical communication," Optics Express, vol. 17, No. 6,pp. 4355-4359, March 2009.

[19] Kazwa Ohsawa and Toshiaki Shibata, " Preparation and Characterization of ZrF4-BaF2-LaF3-NaF-AlF3 Glas Optical Fibers," Journal of Lightwave Technology, vol. LT-2, no. 5, pp. 602-602, October 1984.

[20] Rick K. Nubling and James A. Harrington, "Optical properties of single-crystal sapphire fibers," Applied Optics, vol. 36, no. 24, pp.5934–5940, August 1997.

[21] S.H. Groves, K.W. Nills, J. strauss, "Double heterostructure Pb1-xSnx Te-PbTe lasers with cw operation at 77 K," Applied Physics Letters, vol. 25, No.6,pp. 331-333, September 1974.

[22] Eli Kapon, Semiconductor Lasers II Materials and Structures, Academic Press, 1999.

[23] H.K. Choi, S. J. Eglash, "High power multiple quantum well GaInAsSb/AlGaAsSb diode lasers emitting at 2.1 µm with low threshold current density," Appllied Physics Letter, vol.61, no. 10, pp.1154–1156, September1992.

[24] C. Mourad, D. Gianardi, K. J. Malloy, and R. Kaspi, "2 µm GaInAsSb/AlGaAsSb midinfrared laser grown digitally on GaSb by modulated-molecular beam epitaxy," Journal of Applied Physics, vol.88, no.10, November 2000.

[25] I. Vurgaftman, J.R. Meyer, and L.R. Ram-Mohan, " Band parameters for III-V compound semiconductors and their alloys," Journal of Applied Physics, vol. 89, no. 11, pp. 5815-5875, June 2001.

[26] S.W. McCahon, S.A. Anson, D.-J. Jang, M.E. Flatte, Thomas F. Boggess, D.H. Chow and T.C. Hasenberg, C.H. Grein, " Carrier recombination dynamics in a (GaInSb/InAs)/AlGaSb superlattice multiple quantum well," Applied Physics letter, vol. 68 no.15, pp. 2135-2137, April 1996.

[27] Paul Harrison, Quantum wells, wires and dots, Wiely Interscience; Second Edition 2005.

[28] G. R. Nash, S. J. B. Przeslak, S. J. Smith, G. de Valicourt, A. D. Andreev, P. J. Carrington, M. Yin,A. Krier, S. D. Coomber, L. Buckle, M. T. Emeny, and T. Ashley, "Midinfrared GaInSb/AlGaInSb quantum well laser diodes operating above 200 K," Appllied Physics Letter, vol.94, no.9, pp. 091111, March 2009

[29] G.R. Nash, S. J. Smith, S.D. Coomber, S. Przeslak , A. Andreev, P. Carrington, M. Yin, A. Krier, L. Buckle, M.T. Emeny, and T. Ashley, " Mid-infrared GaInSb/ AlGaInSb quantum well laser diode grown on GaAs," Applied Physics letters, vol. 91, pp. 131118(1-3), September 2007.

[30] Sandra R. Selmic, Tso-Min Chou, JiehPing Sih, Jay B. Kirk, Art Mantie, Jerome K. Butler, David Bour, and Gary A. Evans, "Design and Characterization of 1.3μm AlGaInAs–InP Multiple-Quantum-Well Lasers," IEEE Journal of Selected topics in Quantum Electronics, vol. 7, no. 2, pp. 340-349, March 2001.

[31] S. L. Chuang, Physics of optoelectronics devices, John wiely & sons, 1995.

[32] Atsuko Niwa, Tsukuru Ohtoshi, and Takao Kuroda, "Orientation Dependence of Optical Properties in Long Wavelength Strained Quantum-Well Lasers," IEEE

Journal of Selected topics in Quantum Electronics, vol. 1, no. 2, pp. 211-217, June 1995.

[33] T. Ohtoshi, T. Kuroda, A. Niwa, and S. Tsuji," Dependence of optical gain on crystal orientation in surface-emitting lasers with strained quantum wells", Appllied Physics Letter, vol. 65, no.15, pp. 1886-1888, October 1994.

[34] D.L Smith and C. Mailhiot, "Piezoelectric effects in strained-layer superlattices," Journal of Applied Physics, vol. 63, no.8, pp. 2717-2719, April 1988.

[35] G. Bastard, E.E. Mendez, L.L. Chang, and L. Esaki, "Variational calculations on quantum well in an electric field," Physical Review B, vol. 28, no.6, pp. 3241-3245 September 1983.

[36] Y.K. Kuo, J.R. Chen, M.L. Chen, B. T. Liou, " Numerical study on strained InGaAsP/InGaP quantum wells for 850nm vertical cavity surface emitting lasers," Applied Physics B, DOI:10.1007/s00340-006-2567-5, 2007.

[37] Giammarco Rossi, Roberto Paoletti, Marina Meliga, " SPICE simulation for analysis and design of fast 1.55 μm MQW laser diodes," Journal of lightwave technology, vol. 16, no. 8, pp. 1509-1516, August 1998.

[38] L.A. Coldren, S.W. Corzine, Diode Laser and Photonic Integrated Circuits, Jone Wiely and Sons.

[39] Randall S. Geels, Scott W. Corzine, Larry A. Coldern, " InGaAs Vertical CavitySurface-Emitting Lasers," IEEE Journal of Quantum Electronics, vol. 27, no.6, June 1994.

[40] Daniel F. Feezell , "Long-Wavelength Vertical-Cavity Surface-Emitting Lasers with Selectively Etched Thin Apertures," PhD thesis, University of California, Santa Barbara, 2005.

[41] I. Vurgaftman, J.R. Meyer and L.R. Ram-Mohan, " Band Parameters for III-V compound semiconductors and their alloys", Journal of Applied Physics, vol. 89, no.11, pp. 5815-5875, June 2001.

[42] Sadao Adachi, " Band gaps and refractive indices of AlGaAsSb, GaInAsSb, and InPAsSb: key properties for a varity of the 2-4μm optoelectronic device applications," Journal of Applied Physics, vol.61, no.10, pp. 4869-4876, May 1987.

List of Publications on this dissertation

[1] Md. Mahbub Hasan and Md. Rafiqul Islam, "Strain and Crystal Orientation-dependent Optical Properties of Mid-infrared GaSb-based Quantum Well Laser," Communications and Photonics conference and Exhibition, 2-6 November.2009. URL: http://ieeexplore.ieee.org/stamp/stamp.jsp?tp=&arnumber=5377076&isnumber=5376978.

[2] Md. Mahbub Hasan and Rafiqul Islam, "Strain-dependent Optical Properties of Mid-infrared GaInSb/GaInAlSb Quantum Well Laser," International Conference on Computer and Communication Engineering (ICCCE 2010), 11-13, May 2010, Kuala Lumpur, Malaysia.IEEE Catalog Number: CFP10390-CDR, ISBN: 978-1-4244-6234-6.

[3] Md. Mahbub Hasan and Rafiqul Islam, "Crystal Orientation-dependent Optical Properties of Mid-infrared GaInSb/GaInAlSb Quantum Well Laser," International Conference on Computer and Communication Engineering (ICCCE 2010), 11-13, May 2010, Kuala Lumpur, Malaysia.IEEE Catalog Number: CFP10390-CDR, ISBN: 978-1-4244-6234-6.